Available online at www.sciencedirect.com

ScienceDirect

Advances in Space Research 70 (2022) 1737–1760

ADVANCES IN SPACE RESEARCH (a COSPAR publication)

www.elsevier.com/locate/asr

Validation and calibration of models to estimate photosynthetically active radiation considering different time scales and sky conditions

Marian de Blas [a], Ana García-Rodríguez [b], Ignacio García [a,*], José Luis Torres [a]

[a] Institute of Smart Cities (ISC), Department of Engineering, Public University of Navarre, Campus Arrosadía, 31006 Pamplona, Spain
[b] Research Group Solar and Wind Feasibility Technologies (SWIFT), Electromechanical Engineering Department, University of Burgos, 09006 Burgos, Spain

Received 2 January 2022; received in revised form 13 May 2022; accepted 3 July 2022
Available online 8 July 2022

Abstract

Photosynthetically Active Radiation (*PAR*) is a fundamental parameter for developing plant productivity models. Nevertheless, instrumentation for measuring *PAR* and to record it is scarce at conventional meteorological stations. Several procedures have therefore been proposed for *PAR* estimation. In this work, 21 previously published analytical models that correlate *PAR* with easily available meteorological parameters are collected. Although longer time scales were considered in the original publications, a minute range was applied in this work to calibrate the *PAR* models. In total, more than 10 million input records were gathered from the SURFRAD station network from a 10-year long time series with data frequencies recorded every 1 min. The models were calibrated both globally, using data from all stations and locally, with data from each station. After calibration, the models were validated for minute, hourly and daily data, obtaining low fitting errors at the different stations in all cases, both when using the globally calibrated models and with the models calibrated for each location. Although the *PAR* results in general improved for locally calibrated models, the use of local models is not justified, since the global models presented offered very satisfactory *PAR* results for the different climatic conditions where the meteorological stations are located. Thus, *PAR* estimation model should then be selected, solely considering the meteorological variables available at the specific location. When applying the globally calibrated models to input data classified according to sky conditions (from clear to overcast), the *PAR* models continued to perform satisfactorily, although the error statistics of some models for overcast skies worsened.

Keywords: Photosynthetically active radiation; Solar irradiance; Sky types; Model calibration

1. Introduction

Photosynthetically Active Radiation (*PAR*) incident on the vegetal canopy is one of the basic parameters for the characterization of plant growth behavior, as plants use energy from solar radiation, emitted within the 400 and 700 nm spectral range, to activate photosynthesis that transforms solar into chemical energy.

The intensity of *PAR* that plants process is a key parameter to construct productivity models and cultivation strategies aimed at optimizing the use of energy. A number of published references considered the *PAR* levels that crops process as an input to model the behavior of mixed plantations: coconut/corn (Dauzat and Eroy, 1997), maize/peanut (Awal et al., 2006), wheat/cotton (Zhang et al., 2008), maize/soybean (Liu et al., 2018). Research

* Corresponding author.
E-mail address: ignacio.garcia@unavarra.es (I. García).

https://doi.org/10.1016/j.asr.2022.07.005
0273-1177/

Nomenclature

AIC	Akaike In formation Criterion
BIC	Bayesian Information Criterion
MPE	Mean Percentage Error (%)
PAR	Photosynthetically Active Radiation, expressed either in irradiance units ($W \cdot m^{-2}$) or as photon flux density (PPFD) ($\mu mol \cdot m^{-2} \cdot s^{-1}$)
RMSE	Root Mean Squared Error($W \cdot m^{-2}$)
RMSEr	Relative Root Mean Squared Error (%)
RSD	Relative Standard Deviation (%)
BSRN	Baseline Surface Radiation Network
NIR	Near InfraRed irradiance ($W \cdot m^{-2}$)
QC	Quality Control
Cle	Cloudless index
E_i	Calculated value of *PAR* ($W \cdot m^{-2}$)
E_{avg}	Average of calculated values of *PAR* ($W \cdot m^{-2}$)
G	Global solar horizontal irradiance ($W \cdot m^{-2}$)
G_0	Extra-terrestrial horizontal irradiance ($W \cdot m^{-2}$)
G_d	Diffuse solar horizontal irradiance ($W \cdot m^{-2}$)
G_{0n}	Extra-terrestrial normal irradiance ($W \cdot m^{-2}$)
G_{bn}	Direct solar normal irradiance ($W \cdot m^{-2}$)
G_{sc}	Solar Constant (preset value 1361.1 $W \cdot m^{-2}$)
M_i	Measured value of *PAR* ($W \cdot m^{-2}$)
M_{avg}	Average of measured values of *PAR* ($W \cdot m^{-2}$)
N	Total number of *PAR* data
P_0	Extra-terrestrial Photosynthetically Active Radiation on a horizontal surface ($W \cdot m^{-2}$)
P_{sc}	Solar Constant of Photosynthetically Active Irradiance (preset value 530.8 $W \cdot m^{-2}$)
RH	Relative humidity (%)
R^2	Determination coefficient
SG	Standard global irradiance
Si	Sky Index (Igawa, 2014)
T	Air temperature (°C)
T_d	Dew point temperature (°C)
e	Vapor pressure (hPa)
k_T	Clearness index (G/G_0)
k_c	Clear sky index
k_d	Diffuse fraction or cloud ratio (G_d/G)
k_{ds}	Standard cloud ratio
m	Relative optical air mass
w	Precipitable water (cm)
α_s	Solar altitude (rad)
Δ	Sky's brightness (Perez et al., 1990)
ε	Sky's clearness (Perez et al., 1990)
θ_z	Solar zenith angle (rad)

in the field of plant physiology and ecology has included the value of the incident *PAR* as a key variable for modeling the photosynthetic behavior of plants in response to sunlight (Bhattacharya, 2019; Campillo et al., 2012; Jajoo et al., 2014; Ogburn and Edwards, 2010), for selecting photosynthetically efficient cultivars (Peng et al., 2000), for analyzing the metabolic behavior of aquatic species (O'Gorman et al., 2012) and, in some examples, plant growth and flowering (Bredmose and Costes, 2017).

PAR can be measured in energetic terms ($W \cdot m^{-2}$) or in photobiological units, *i.e.*, in terms of photon flux density ($\mu mol \cdot m^{-2} \cdot s^{-1}$). The Photosynthetic Photon Flux Density (*PPFD*) is the number of photons in the 400–700 nm waveband incident on unit surface area in unit time (Foyo-Moreno et al., 2017). McCree (1972) proposed a widely employed constant ratio of 4.57 $\mu mol \cdot J^{-1}$ between the *PPFD* and the incident *PAR* in terms of energy. Actually, there is a monochromatic relationship between these two variables and, therefore, the integrated broadband photon flux cannot be directly obtained from the global irradiance in the 400–700 nm waveband (Ross and Sulev, 2000; Sun et al., 2017). Notwithstanding, Akitsu et al. (2015) analyzed the dependence of McCree's ratio on climatic factors and considered the constant value acceptable for most purposes.

Existing instruments for measuring *PAR* can be classified into two classes (Mottus et al., 2012): *PAR* quantum photovoltaic sensors that are sensitive to photoelectric effects; and *PAR* energy sensors, which mainly include thermoelectric instruments. In addition, some field instruments of these technologies have been developed for measuring absorbed *PAR* in crops and pastures (Rahman et al., 2014) and for obtaining the daily light integral in greenhouses (Torres and Lopez, 2012). Nevertheless, despite the *PAR* value being a key variable in physiological models of plant growth, there are only a limited number of meteorological stations around the world that provide data with reliable measurements of this parameter for research (Foyo-Moreno et al., 2017). It is also difficult to maintain measurement accuracy and there is no standard for the quality control of *PAR* measurements (Mizoguchi et al., 2010; Mizoguchi et al., 2014).

More often than not, *PAR* is therefore indirectly estimated from other parameters. The physical relationship between *PAR* and global irradiance (G) depends on the absorption and dispersion caused by the atmospheric components such as aerosol, water vapor, ozone, and clouds (Janjai et al., 2015).

Some current *PAR* estimation models include inputs obtained from satellite data (Hao et al., 2020; Janjai et al., 2015; Vindel et al., 2018). Likewise, radiative transfer models use either satellite or terrestrial observations or both (Akitsu et al., 2015; Li et al., 2015; Tang et al., 2017; Wandji Nyamsi et al., 2015; Wandji Nyamsi et al., 2019).

In general, *PAR* results from physical models are very good, but the required input and the application of the

models can be difficult for first-time users. In contrast, semi-empirical models can correlate PAR or the PAR/G ratio with other parameters directly measured at weather stations or derived from weather station data (Aguiar et al., 2012; Alados et al., 1996; Foyo-Moreno et al., 2017; Ge et al., 2011; Hu et al., 2007; Janjai et al., 2015; Li et al., 2010; Mizoguchi et al., 2014; Wang et al., 1961; Yu et al., 2015; Vindel et al., 2018). Various models also use artificial neural network techniques with calculable parameters (Ferrera-Cobos et al., 2020; García-Rodríguez et al., 2021; Jacovides et al., 2015; Wang et al., 2016; Zempila et al., 2016).

The models cited above considered a time scale ranging from 10 min to monthly PAR values. Literature reviews revealed that the fitting quality of the different models varied as a function of meteorological, seasonal, and geographic characteristics of locations. The correlation between PAR and the meteorological parameters also differed, depending on the local conditions (García-Rodríguez et al., 2020; García-Rodríguez et al., 2021; Wang et al., 2016). An exhaustive review of empirical models for PAR estimation can be found in Nwokolo and Amadi (2018).

In the study by Li et al. (2010), the PAR/G ratio increased under high humidity or cloudy conditions, because water vapor content in the atmosphere increases the absorption of radiation in the NIR spectrum, whereas the absorption of radiation is unaffected in the PAR region. Yu et al. (2015) analyzed the influence of parameters on semi-empirical models using experimental PAR data from the Surface Radiation Budget Network (SURFRAD) for a daily temporal resolution. They observed a high correlation between daily PAR/G and the clearness index (k_T), *i.e.*, the global solar horizontal irradiance over the corresponding extra-terrestrial irradiance (G/G_0). This ratio denoted high values for low k_T and vice versa. Likewise, a negative correlation was obtained between the PAR/G ratio and the cosine of the solar zenith angle ($\cos\theta_z$) and dew point temperature (T_d) and a positive correlation between that ratio and both the diffuse fraction (k_d) and the sky's brightness (Δ) values. They also concluded, unlike other published research, that the dew point value, used to describe atmospheric humidity, had no significant influence on the PAR/G ratio.

A physical model was published (Sun et al., 2017) to estimate PAR from both global and direct radiation in the spectral region between 200 and 700 nm. This model was validated using data with a 1-min temporal resolution that included a part of the experimental PAR data used in the present research.

In general, the semi-empirical models reported in the literature yielded accurate results, by means of a simple mathematical expression, when applied under local conditions similar to those considered for calibration. In contrast, the transferability of models to other locations and their local adaptation still needs further discussion (García-Rodríguez et al., 2021).

When the calibration site and the location of interest have comparable atmospheric conditions, it is expected that the atmospheric conditions in both places will cause a similar attenuation of solar radiation in the PAR wavelength range. Therefore, the model for PAR determination should produce accurate results. Different coefficients in similar equations have been proposed, to take into account the sky conditions (Ferrera-Cobos et al., 2020; Jacovides et al., 2007; Wang et al., 1961; Yu et al., 2015).

In this work, 21 models for PAR estimation were calibrated and evaluated. For this purpose, a 10-year long series of 1-min resolution data was configured from data recorded at seven weather stations within the SUFRAD network, covering a wide range of climatic conditions in the USA. The main objective of this work is to present models that can be generally applied and that provide accurate PAR values using meteorological variables measured at ground stations and considering time intervals between one minute and one day. An objective that was achieved with a data set of more than 10 million PAR and meteorological measurements that are representative of a large variety of regional and weather conditions.

The expected errors in PAR estimation when the 21 models under analysis were applied, were firstly quantified for all sky conditions together and then considering the prevailing sky conditions. By doing so, users who need to know the PAR at a given location are provided with a set of easy-to-implement equations and they can select the most appropriate model, depending on the available meteorological input data. In order to analyze the effect of local climatic conditions on PAR estimation, models were also calibrated using data from each particular weather station and the obtained PAR values were compared with PAR resulting from applying the globally calibrated models at each location.

This paper is organized into five sections. The meteorological data and its classification in sky types are detailed in Section 2. In Section 3, the PAR models and the calibration procedure is described. The calibrated models for the minute-time scale and the statistical analysis of the results when the models were applied to three-time scales (minute, hourly, and daily) and to different sky types are presented in Section 4. Finally, the conclusions are detailed in Section 5.

2. Weather data

We used high quality datasets retrieved from the Surface Radiation Budget Network (SURFRAD) FTP Server based in the United States: PAR on the horizontal plane, global and diffuse solar irradiance on the horizontal plane, air temperature and relative humidity.

Global PAR was measured with an LI-COR Quantum sensor within the 400 to 700 nm broadband range. PAR values are given in $W \cdot m^{-2}$. The G values were obtained from a Spectrolab SR-75 pyranometer and diffuse irradi-

ance was measured on the horizontal plane with an Eppley 8–48 pyranometer. Both pyranometers measure data within the 280–3000 nm broadband range.

The seven stations belonging to the SURFRAD network are distributed throughout different climatic areas in the United States, as shown in Fig. 1. The Köppen-Geiger climate classification map shown in Fig. 1 was extracted form Beck et al. (2018). The ground properties of these stations were described in Wandji Nyamsi et al. (2019). Table 1 shows the geographical location and the basic climatic data from the seven weather stations.

All the SURFRAD stations never started to take measures at the same time. The earliest radiation measurements were taken in 1995 and the latest, in 2003. Notwithstanding, with the aim of comparing similar series of data for model calibration purposes, we considered a common time range of records between 1/1/2009 and 31/12/2018 at every station, with a temporal resolution of 1 min. Irradiance data collected at the stations within the network had previously passed the Baseline Surface Radiation Network (BSRN) quality control checks, as explained in Long and Dutton (2002). Unfortunately, criteria for Quality Control (QC) of *PAR* are neither covered in the BSRN procedures or in any assessment standards we have consulted in the bibliography available to us. Therefore, an in-house QC method described below was set in accordance with the physical limits of *PAR*. Global *PAR* on the horizontal plane cannot be higher than extraterrestrial *PAR* on the horizontal plane corresponding to the same time. Extraterrestrial *PAR* on the horizontal plane (P_0) is calculated with the correction factor (f_c) applied to the *PAR* solar constant (P_{sc}) that takes into account the eccentricity of the Earth's orbit and then multiplies the result by the cosine of the solar zenith angle, Eq. (1).

$$P_0 = f_c P_{sc} \cos\theta_z. \tag{1}$$

Gueymard (2018) obtained a value of 1361.1 $W \cdot m^{-2}$ for the solar constant (G_{sc}), but no standardized value for the irradiance in the *PAR* spectral range. Thus, the irradiance curve between 400 and 700 nm of the extraterrestrial spectrum proposed by Gueymard et al. (2002) was integrated, in order to estimate this constant, resulting in a value of 530.8 $W \cdot m^{-2}$. Gueymard's extraterrestrial spectrum is proposed to determine the reference AM1.5 spectrum specified in standard IEC 60904–3:2019 (IEC, 2019). Data corresponding to solar elevation angles lower than 5° were discarded to avoid the cosine response problems of global irradiance and *PAR* measuring instruments. Table 2 shows the number of data initially available at each station and the number of records that passed the QC checks.

Data were classified into five sky types according to the Sky Index (*Si*), Eq. (2), proposed by Igawa (2014) that can be seen in Table 3. This classification allowed us to analyze the influence of a given atmospheric condition, represented by the sky type, on the behavior of the models to be evaluated.

$$Si = \sqrt{(1-k_c)^2 - \left(1 - Cle^{0.5}\right)^2}, \tag{2}$$

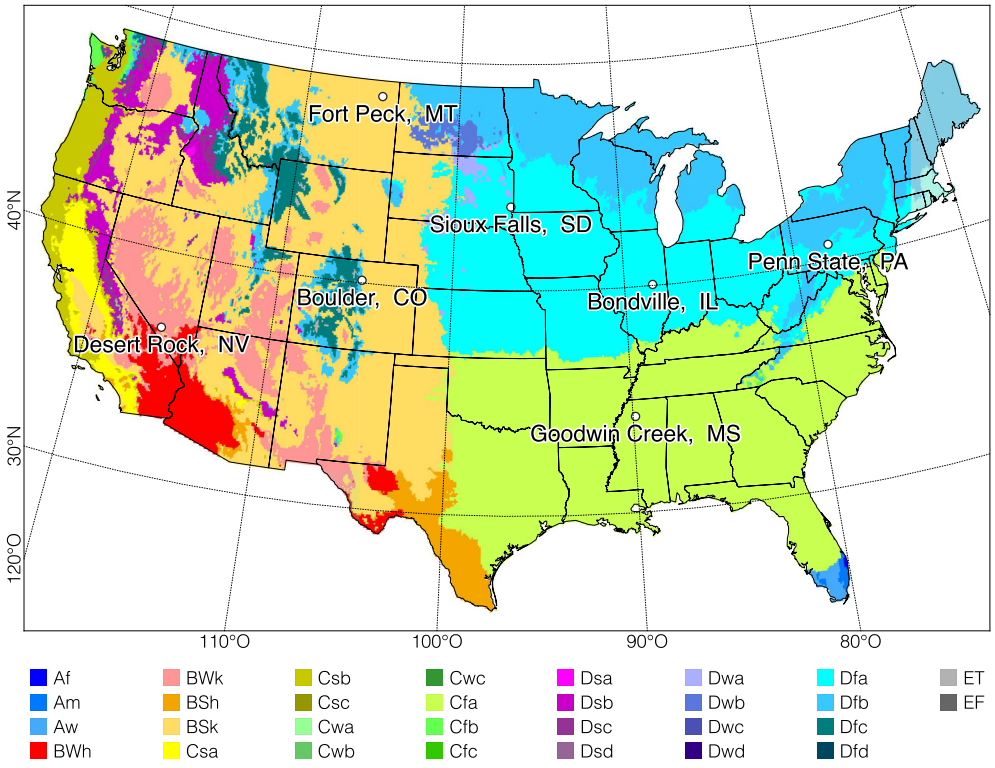

Fig. 1. Locations of the seven SURFRAD stations. Köppen-Geiger climate classification map extracted form Beck et al. (2018).

Table 1
Geographical location and basic climatic data from the seven SURFRAD weather stations.

Station	Code	Latitude (°N)	Longitude (°W)	Elevation (m)	Average temperature (°C)	Average relative humidity (%)	Average G ($W \cdot m^{-2}$)	Average PAR ($W \cdot m^{-2}$)	Köppen-Geiger class (*)
Bondville, Illinois	BON	40.0519	88.3731	230	11.53	72.65	170.46	73.82	Dfa
Table Mtn., Boulder, Colorado	TBL	40.1250	105.237	1689	12.25	46.92	193.71	84.29	Bsk
Desert Rock, Nevada	DRA	36.6237	116.019	1007	18.81	28.04	235.18	104.22	Bwk
Fort Peck, Montana	FPK	48.3078	105.102	634	5.84	67.24	161.89	72.66	Bsk
Goodwin Creek, Mississippi	GWN	34.2547	89.8729	98	16.73	71.89	182.14	79.07	Cfa
Penn. State Univ., Pennsylvania	PSU	40.7201	77.9309	376	10.52	70.01	152.83	65.73	Dfa
Sioux Falls, South Dakota	SXF	43.734	96.6233	473	7.96	73.13	166.50	74.40	Dfa

(*) Bwk (arid, desert, cold), Bsk (arid, steppe, cold), Cfa (temperate, no dry season, hot summer), Dfa (cold, no dry season, hot summer).

where k_c is the clear sky index, Eq. (3), and Cle is the cloudless index calculated by Eq. (7).

$$k_c = G/SG. \tag{3}$$

$$Cle = (1 - k_d)/(1 - k_{ds}), \tag{4}$$

where G is the global horizontal irradiance, SG the standard global irradiance, calculated by Eq. (5), k_d the diffuse fraction (G_d/G), referred to as cloud ratio by Igawa (2014), and k_{ds} the standard cloud ratio, Eq. (6).

$$SG = \frac{0.84 G_{sc}}{m \exp(-0.054m)}. \tag{5}$$

$$k_{ds} = 0.08302 + 0.5358 \exp -17.3\alpha_s + 0.3818 \times \exp -3.2899\alpha_s, \tag{6}$$

where m the relative optical air mass (Kasten and Young, 1989) and α_s is the solar altitude, expressed in radians.

Table 4 shows the number of available measurements at each station to calibrate and to validate PAR estimation models after having passed the QC. Calibration of a model implies using 50% of the data, alternatively chosen, for the model calibration and 50% to validate the resulting expressions.

SURFRAD stations register a large number of meteorological variables, but only those necessary for the application of the models described in Section 3 were considered in this paper: global PAR on the horizontal plane (PAR), global (G) and diffuse (G_d) horizontal irradiance, and air temperature (T) and relative humidity (RH). However, various models consider the atmospheric water vapor content by means of the dew point (T_d), the vapor pressure (e) or the precipitable water content (w). These parameters are not directly registered in the stations; hence they were estimated on the basis of T and RH. T_d and e were calculated according to Eqs. (7) and (8).

$$T_d = \frac{243.04\left(\ln\left(\frac{RH}{100}\right) + \frac{17.625T}{T+243.04}\right)}{17.625 - \ln\left(\frac{RH}{100}\right) - \frac{17.625T}{T+243.04}}. \tag{7}$$

$$e = 6.11 \frac{RH}{100} \cdot 10^{\frac{7.5T}{T+237.3}}. \tag{8}$$

The precipitable water content (w) was obtained from Leckner (1978), according to Eq. (9).

$$w = \frac{0.00493 e_s RH}{T + 273.15}. \tag{9}$$

w depends on the partial pressure of water vapor in saturated air (e_s), calculated by Eq. (10).

$$e_s = \exp\left(26.23 - \frac{5416}{T + 273.15}\right). \tag{10}$$

Some of the analyzed models also depend on one or both of the variables proposed by Perez et al. (1990) to parameterize the sky conditions, *i.e.*, the sky's clearness and brightness. The sky's clearness (ε) can be calculated according to Eq. (11).

Table 2
Total number of records available at each SURFRAD network station and number of records that passed the QC checks.

	Station						
	BON	DRA	FPK	GWN	PSU	SXF	TBL
Available data ($\theta_z < 85°$)	1,501,535	1,769,842	2,130,006	1,627,176	1,634,785	1,440,148	1,602,364
Data passing QC	1,371,257	1,545,048	1,852,600	1,363,076	1,478,690	1,310,735	1,413,606
Data passing QC (%)	91.32	87.30	86.98	83.77	90.45	91.01	88.22

Table 3
Sky classification according to the Sky Index (Si) proposed by Igawa (2014).

Sky classification	Sky Index (Si)
Clear Sky (Clear)	<0.15
Intermediate Clear Sky (I-Clear)	$0.15 \leqslant Si < 0.3$
Intermediate Sky (Intermediate)	$0.3 \leqslant Si < 0.9$
Intermediate Overcast Sky (I-Overcast)	$0.9 \leqslant Si < 1.15$
Overcast Sky (Overcast)	$Si \geqslant 1.15$

$$\varepsilon = \frac{\frac{(G_d+G_{bn})}{G_d} + 1.041\theta_z^3}{1 + 1.041\theta_z^3}, \tag{11}$$

where G_{bn} is the direct normal irradiance and the solar zenith angle (θ_z) should be expressed in radiands.

The sky's brightness (Δ) is given by Eq. (12).

$$\Delta = \frac{mG_d}{G_{0n}}, \tag{12}$$

where G_{0n} is the extra-terrestrial normal irradiance.

3. Methodology

Table 5 shows the mathematical expressions corresponding to the 21 models considered in this work for estimating PAR and their corresponding source. Models M1 to M10 for the PAR/G fraction were previously calibrated by Yu et al. (2015), considering daily values obtained from the SURFRAD network over the period between 2009 and 2010 and for all sites and all sky conditions together. The resulting R^2 values ranged from 0.4599 (M5) to 0.5475 (M10), which are low values for this parameter, and RMSE values (in $MJ \cdot m^{-2}$) from 0.02131 (M9) to 0.02326 (M7). It should be noted that Yu et al. (2015) attributed models M5 to M10 to various authors, but on consulting the referenced publications, it was found that the models and the citations could not be cross-referenced. In this work, we have therefore attributed the models whose original reference is uncertain to Yu et al. (2015).

We downloaded 10,335,012 data items (Table 3) from all stations that had passed the QC to conduct the calibration process described in this work and to fit the results of models M1 to M21. All the models were fitted for PAR (in $W \cdot m^{-2}$) and not for the PAR/G fraction, in order to achieve homogeneity. However, models M1 to M13 and M19 were originally published considering PAR/G as the dependent variable. A 1-min time base was used to adjust the models, because the PAR values obtained with this frequency were thought to provide users with useful input data for later studies that might require in-depth analysis. The behavior of the models obtained from the adjustment considering an hourly basis was also evaluated, since data from the input parameters required in the models is often available at this frequency. Furthermore, 1-day input data

Table 4
Total data and data classified according to the sky type that have passed the quality control and the solar minimum elevation parameter for each station. Time series includes data from 2009 to 2018.

Station	All sky	Clear	I-Clear	Intermediate	I-Overcast	Overcast
BON	1,371,257	636,401	259,743	352,698	105,381	17,034
%	100	46.41	18.94	25.72	7.68	1.24
DRA	1,852,600	1,399,386	185,258	214,100	49,715	4,141
%	100	75.54	10	11.56	2.68	0.22
FPK	1,363,076	682,583	232,362	323,409	108,049	16,673
%	100	50.08	17.05	23.73	7.93	1.22
GWN	1,478,690	700,298	265,390	340,367	138,794	33,841
%	100	47.36	17.95	23.02	9.39	2.29
PSU	1,310,735	490,228	216,272	348,225	200,990	55,020
%	100	37.4	16.5	26.57	15.33	4.2
SXF	1,413,606	701,128	229,540	327,663	130,533	24,742
%	100	49.6	16.24	23.18	9.23	1.75
TBL	1,545,048	883,883	182,998	314,297	138,336	25,534
%	100	57.21	11.84	20.34	8.95	1.65
Total	10,335,012	5,493,907	1,571,563	2,220,759	871,798	176,985
%	100	53.16	15.21	21.49	8.44	1.71

Table 5
Models evaluated for *PAR* estimation.

Model	Expression	Variables	Reference
M1	$PAR = G(a_1 \ln\varepsilon + b_1 \ln\Delta + c_1 T_d + d_1 \cos^2\theta_z + f_1)$	G, ε, Δ, T_d, $\cos\theta_z$	Alados et al. (1996)
M2	$PAR = G(a_2 \ln\varepsilon + b_2 \ln\Delta + c_2 \cos^2\theta_z + d_2)$	G, k_d, Δ, $\cos\theta_z$	Alados et al. (1996)
M3	$PAR = G(a_3 \ln k_T + b_3 T_d + c_3 \cos\theta_z + d_3)$	G, k_T, T_d, $\cos\theta_z$	Alados et al. (1996)
M4	$PAR = G(a_4 \ln k_T + b_4 \cos\theta_z + c_4)$	G, k_T, $\cos\theta_z$	Alados et al. (1996)
M5	$PAR = G(a_5 \ln k_T + b_5)$	G, k_T	Wandji Nyamsi et al. (2019)
M6	$PAR = G\left[a_6(\ln k_T)^2 + b_6 \ln k_T + c_6\right]$	G, k_T	Yu et al. (2015)
M7	$PAR = G(a_7 \ln k_d + b_7 \ln\Delta + c_7)$	G, Δ, k_d	Yu et al. (2015)
M8	$PAR = G\left[a_8(\ln k_T)^2 + b_8 \ln k_T + c_8 T_d + d_8\right]$	G, k_T, T_d	Yu et al. (2015)
M9	$PAR = G\left[a_9(\ln k_T)^2 + b_9 \ln k_T + c_9 \cos\theta_z + d_9\right]$	G, k_T, $\cos\theta_z$	Yu et al. (2015)
M10	$PAR = G\left[a_{10}(\ln k_T)^2 + b_{10} \ln k_T + c_{10} T_d + d_{10} \cos\theta_z + f_{10}\right]$	G, k_T, T_d, $\cos\theta_z$	Yu et al. (2015)
M11	$PAR = G(a_{11} \ln\varepsilon + b_{11} \ln\Delta + c_{11} \ln w + d_{11} \cos\theta_z + f_{11})$	G, ε, Δ, w, $\cos\theta_z$	Hu et al. (2007)
M12	$PAR = G(a_{12} \ln\varepsilon + b_{12} \ln\Delta + c_{12} \cos\theta_z + d_{12})$	G, ε, Δ, $\cos\theta_z$	Hu et al. (2007)
M13	$PAR = G(a_{13} \ln k_T + b_{13} w + c_{13} \cos\theta_z + d_{13})$	G, k_T, w, $\cos\theta_z$	Hu et al. (2007)
M14	$PAR = \left(a_{14} k_T + b_{14} k_T^2 + c_{14} k_T^3 + d_{14}\right)(\cos\theta_z)^{f_{14}}$	k_T, $\cos\theta_z$	Wang et al. (1961)
M15	$PAR = a_{15} k_T \cos\theta_z$	k_T, $\cos\theta_z$	Foyo-Moreno et al. (2017)
M16	$PAR = a_{16} G + b_{16}$	G	Aguiar et al. (2012)
M17	$PAR = a_{17} G + b_{17} k_T + c_{17}$	G, k_T	Aguiar et al. (2012)
M18	$PAR = a_{18} G + b_{18} k_T + c_{18}\Delta e + d_{18}$	G, k_T, Δ, e	Aguiar et al. (2012)
M19	$PAR = G(a_{19} \ln k_T + b_{19} \ln m + c_{19} e + d_{19})$	G, k_T, m, e	Mizoguchi et al. (2014)
M20	$PAR = a_{20} G + b_{20} G \cos\theta_z + c_{20} G k_T + d_{20}$	G, k_T, $\cos\theta_z$	Ge et al. (2011)
M21	$PAR = a_{21} k_T \cos\theta_z + b_{21}$	k_T, $\cos\theta_z$	Variation of M15

were also considered for testing the models, since the results may be of interest for comparison with other previous studies where daily *PAR* values were obtained.

In order to evaluate the dependence of the models on the local conditions of each station, two analyses were performed. First, the behavior of each of the 21 globally fitted models –considering all the stations of the SURFRAD network– was evaluated for each of the stations. Secondly, a local calibration of the models was carried out using data from each site. In this way, it was possible to compare the performance of the locally fitted models with the global ones. It should be remembered that, in all cases, the distribution of data for calibration and validation was carried out according to the criterion described in Section 2, *i.e.*, half of the dataset for calibration and the other half for validation.

The following statistics, described by Eqs. (13)–(17), were used for the validation of the models:

- Determination coefficient:

$$R^2 = \frac{\sum_{i=1}^{N}(E_i - E_{avg})(M_i - M_{avg})}{\left\{\left[\sum_{i=1}^{N}(E_i - E_{avg})^2\right]\left[\sum_{i=1}^{N}(M_i - M_{avg})^2\right]\right\}^{0.5}}. \quad (13)$$

- Root Mean Squared Error:

$$RMSE = \left[\frac{1}{N}\sum_{i=1}^{N}(E_i - M_i)^2\right]^{0.5}. \quad (14)$$

- Relative Root Mean Squared Error:

$$RMSEr(\%) = \frac{100}{M_{avg}}\left[\frac{1}{N}\sum_{i=1}^{N}(E_i - M_i)^2\right]^{0.5}. \quad (15)$$

- Relative Standard Deviation:

$$RSD(\%) = \left[\frac{1}{N}\sum_{i=1}^{N}\left(\frac{E_i - M_i}{M_i}\right)^2\right]^{0.5} 100. \quad (16)$$

- Mean Percentage Error:

$$MPE(\%) = \frac{1}{N}\left(\sum_{i=1}^{N}\frac{E_i - M_i}{M_i}\right)100, \quad (17)$$

where E_i is the calculated value, E_{avg} is the mean of the calculated values, M_i is the measured value, M_{avg} is the mean of the measured values and N is the total number of data items.

The Akaike Information Criterion (*AIC*) and the Bayesian Information Criterion (*BIC*), calculated by Wolfram Mathematica® software, were used to measure the relative quality of the models under analysis, in order to select the model that was sufficiently good and simple, *i.e.*, the most parsimonious model. The underlying idea was o find a balance between the goodness of fit of a model and its complexity.

4. Results and discussion

4.1. Globally calibrated models evaluated both globally and locally for each SURFRAD station

Table 6 shows the results of the coefficients for models M1 to M21 globally calibrated, *i.e.*, considering all sites and sky types together.

Due to space reasons, given the length of the results to be shown, the estimation errors obtained by the models

Table 6
Globally calibrated models for *PAR* using 1-min input data from all stations and obtained determination coefficients (R^2).

Model	Calibrated expression	R^2
M1	$PAR = G(-0.0206671\cos^2\theta_z - 0.028342\ln\Delta - 0.0270876\ln\varepsilon + 0.000152279T_d + 0.425525)$	0.9987
M2	$PAR = G(-0.0182345\cos^2\theta_z - 0.0286075\ln\Delta - 0.0280839\ln\varepsilon + 0.425987)$	0.9987
M3	$PAR = G(-0.028706\cos\theta_z - 0.0278875\ln k_T + 0.000129279T_d + 0.437906)$	0.9988
M4	$PAR = G(-0.0258378\cos\theta_z - 0.0295837\ln k_T + 0.435928)$	0.9988
M5	$PAR = G(0.415212 - 0.0350336\ln k_T)$	0.9987
M6	$PAR = G\left(-0.0340535(\ln k_T)^2 - 0.0757318\ln k_T + 0.406944\right)$	0.9987
M7	$PAR = G(0.0336608\ln k_d - 0.0349165\ln\Delta + 0.413051)$	0.9986
M8	$PAR = G\left(-0.0349876(\ln k_T)^2 - 0.0774526\ln k_T - 0.0000716119T_d + 0.406896\right)$	0.9987
M9	$PAR = G\left(-0.02303\cos\theta_z - 0.0197733(\ln k_T)^2 - 0.0538075\ln k_T + 0.428876\right)$	0.9988
M10	$PAR = G\left(-0.0255814\cos\theta_z - 0.0169287(\ln k_T)^2 - 0.0490527\ln k_T + 0.0000967929T_d + 0.431371\right)$	0.9988
M11	$PAR = G(-0.0297581\cos\theta_z - 0.0284931\ln\Delta - 0.0271005\ln\varepsilon + 0.0022675\ln w + 0.435327)$	0.9988
M12	$PAR = G(-0.0264467\cos\theta_z - 0.0287232\ln\Delta - 0.028097\ln\varepsilon + 0.434845)$	0.9987
M13	$PAR = G(-0.0279869\cos\theta_z - 0.0281807\ln k_T + 0.000938004w + 0.436261)$	0.9988
M14	$PAR = (\cos\theta_z)^{0.928878}(-167.836k_T^3 + 202.545k_T^2 + 481.162k_T + 16.7594)$	0.9987
M15	$PAR = 574.278k_T\cos\theta_z$	0.998
M16	$PAR = 0.413286G + 8.38447$	0.9939
M17	$PAR = 0.414235G - 1.94159k_T + 9.13333$	0.9939
M18	$PAR = 0.0885944e + 0.41312G - 0.0993371k_T + 7.6279$	0.994
M19	$PAR = G(0.000155103e - 0.0277219\ln k_T + 0.0176706\ln m + 0.409838)$	0.9988
M20	$PAR = 0.474298G - 0.0196574G\cos\theta_z - 0.0483035Gk_T + 1.403$	0.9943
M21	$PAR = 550.309k_T\cos\theta_z + 11.5173$	0.9929

are included in Appendix A. Table A.1 shows the statistical results derived from the fit of the experimental data with the theoretical models at minute frequency. Experimental data were evaluated for all sites together and by station, in order to analyze the local effect. All the models yielded very satisfactory fitted results, with values of R^2 over 0.99. When 1-min frequency was considered for input data, *RMSE* values ranged from 8.416 $W \cdot m^{-2}$ in M10 to 10.93 $W \cdot m^{-2}$ in M15 for all sites together. At the stations BON, PSU and TBL with Dfa climate (cold, no dry season, hot summer), *RMSE* values ranged between 7.451 $W \cdot m^{-2}$ (M10) and 11.742 $W \cdot m^{-2}$ (M15). At GWN station with Cfa climate (temperate, no dry season, hot summer), the range of *RMSE* variation was narrower, between 9.034 $W \cdot m^{-2}$ (M10) and 10.307 $W \cdot m^{-2}$ (M15). Two stations (FPK and TBL) are located in Bsk (arid, steppe, cold) climate sites. In this case, *RMSE* values varied between 6.875 $W \cdot m^{-2}$ (M10) and 10.842 $W \cdot m^{-2}$ (M15). At the DRA station located in Bwk climate (arid, desert, cold), *RMSE* ranged from 8.061 $W \cdot m^{-2}$ (M4) to 11.846 $W \cdot m^{-2}$ (M15).

Figs. 2–4 show the *RMSEr* values obtained when globally fitted models M1 to M21 were applied to all sites together and to individual stations, considering time frequencies for input data of 1 min, 1 h, and 1 day. When the globally calibrated models listed in Table 6 were applied on hourly or daily input data, the good quality of the fitted results was maintained; no single model stood out due to its better or worse performance. Only the behavior of the M15 and M21 models was somewhat worse, as was the case in the previous minute-time scale calibration. The obtained *RMSEr* values were somewhat smaller for all models and all time scales at the stations located in arid climate sites (FPK, TBL, DRA) than at those located in more humid sites (SXF, BON, PSU). As can be seen, relative deviations were low, although in some of the models some of the statistics were somewhat higher. Based on these results of the models under study, it cannot be said that there are one or more models that stand out for their good or bad quality. *AIC* and *BIC* values were also used to assess model fit for all sites together but the results obtained were inconclusive.

4.2. Locally calibrated models for each SURFRAD station

Models M1 to M21 were also calibrated from 1-min frequency data at each of the seven stations of the SURFRAD network, representative of different climatic conditions. The locally calibrated models for each station are shown in Tables B.1 to B.7 in Appendix B. This way it was possible to analyze if models fitted for specific local conditions improve the estimates of *PAR*. Table A.2 in Appendix A shows the statistical errors obtained after validation of the fitted models for each station from 1-min data.

Figs. 5–7 show the obtained *RMSEr* values at the different stations when the models, calibrated for each location, were applied to experimental data at 1-min, 1-h and 1-day frequency. In general, the *RMSEr* values obtained decreased at all stations and for all models when the models were calibrated with data corresponding to the locality. However, the improvement of this statistical parameter was not significant when comparing the *RMSEr* values obtained by the models calibrated for all stations together (Figs. 2–4) with that corresponding to the calibration by locality (Figs. 5–7). Thus, for 1-min data, the model with the lowest *RMSEr* at each station in the global calibration

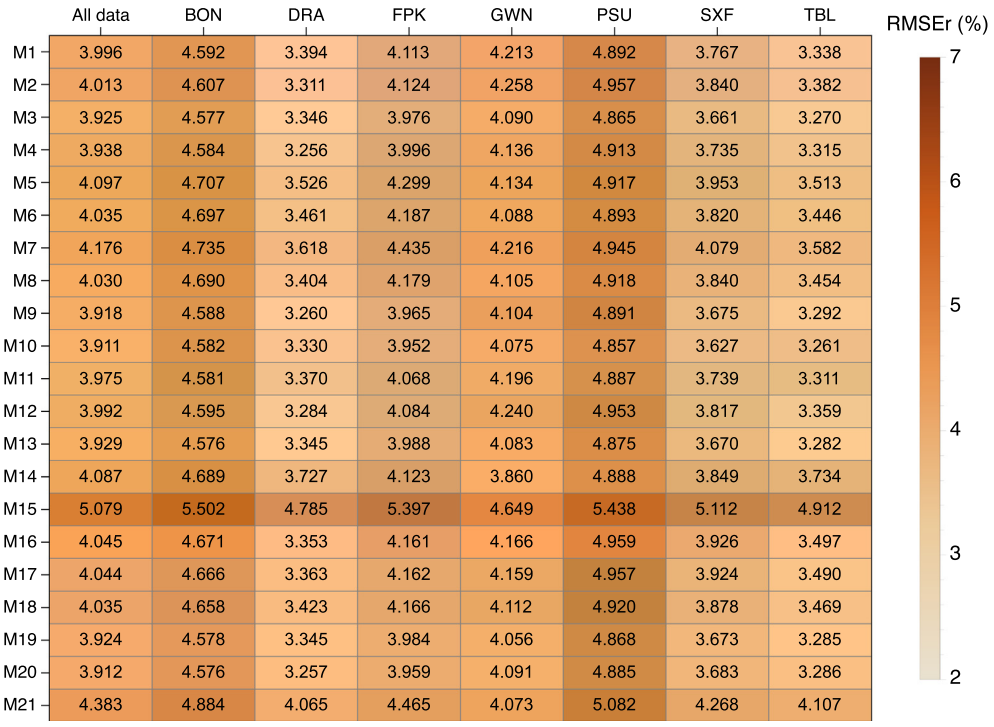

Fig. 2. *RMSEr* values (%) obtained for each model after validation, using 1-min data, of the models fitted globally from 1-min data. The errors obtained globally –considering all sites– and at each SURFRAD station are shown.

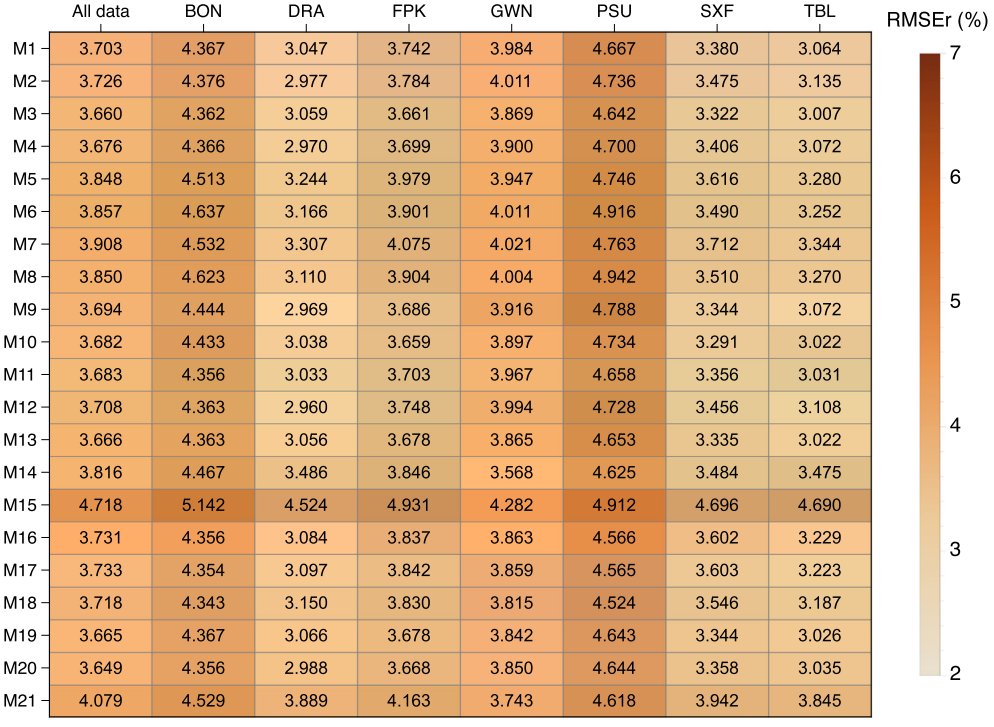

Fig. 3. *RMSEr* values (%) obtained for each model after validation, using 1-h data, of the models fitted globally from 1-min data. The errors obtained globally –considering all sites– and at each SURFRAD station are shown.

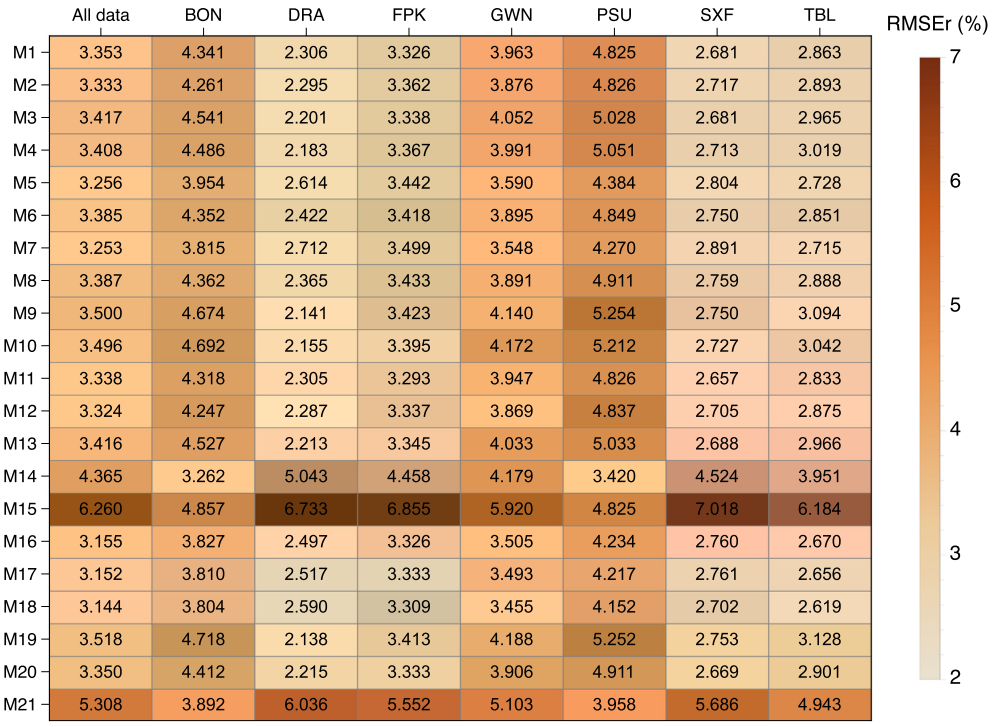

Fig. 4. *RMSEr* values (%) obtained for each model after validation, using 1-day data, of the models fitted globally from 1-min data. The errors obtained globally –considering all sites– and at each SURFRAD station are shown.

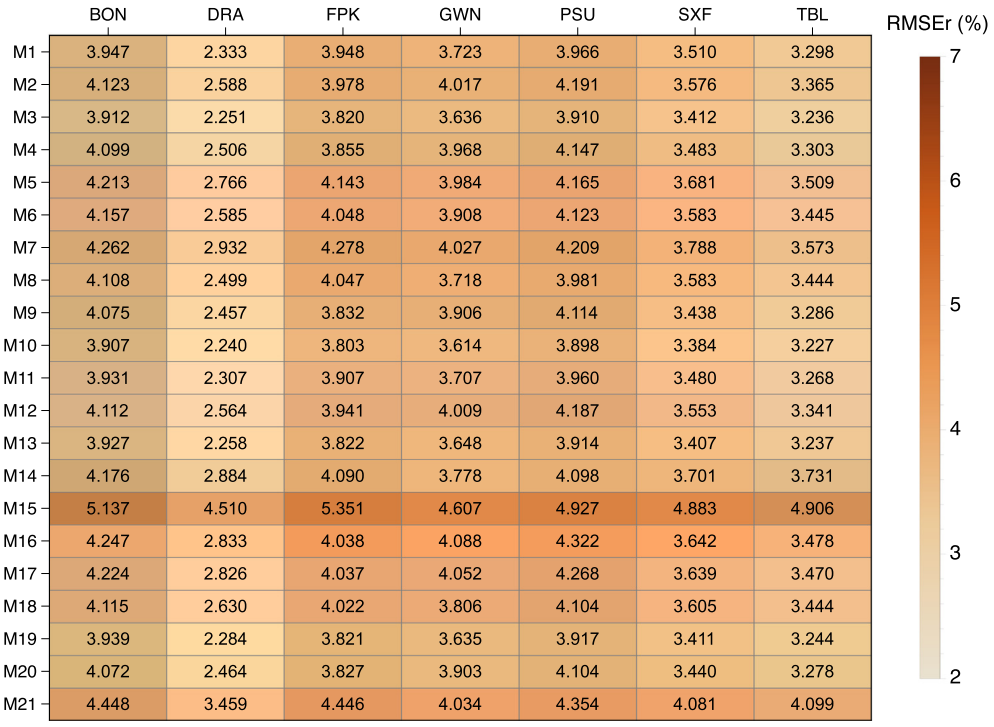

Fig. 5. *RMSEr* values (%) obtained for each model and at each SURFRAD station after validation, using 1-min data, of the models fitted locally from 1-min data.

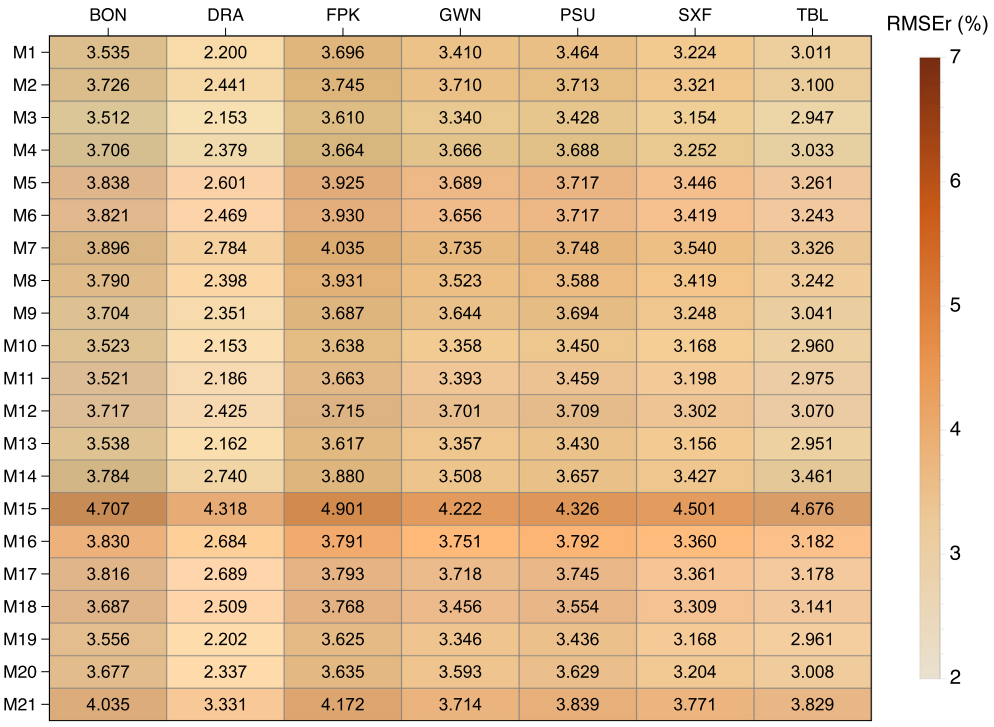

Fig. 6. *RMSEr* values (%) obtained for each model and at each SURFRAD station after validation, using 1-h data, of the models fitted locally from 1-min data.

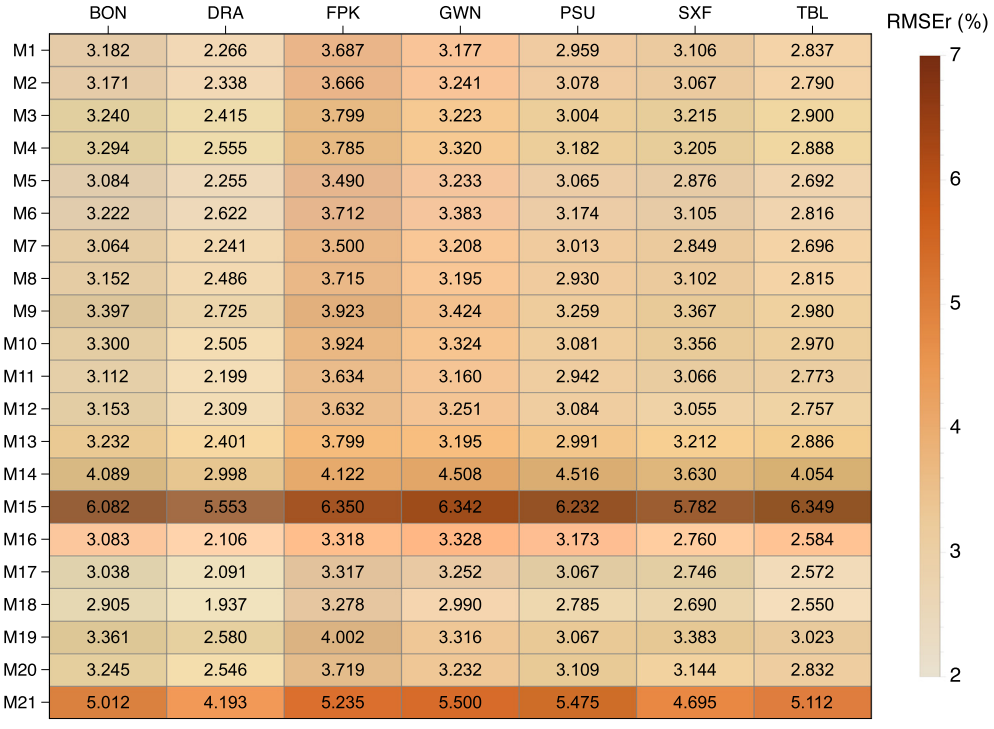

Fig. 7. *RMSEr* values (%) obtained for each model and at each SURFRAD station after validation, using 1-day data, of the models fitted locally from 1-min data.

improved its value from 0.15% to 1%. In the case of the models with the greatest error, the improvement was a maximum of 0.5%. The same behavior was observed for 1-h values. At this frequency, the models that had lower *RMSEr* values for the global calibration, improved this statistic up to 0.94% for local calibration and those with

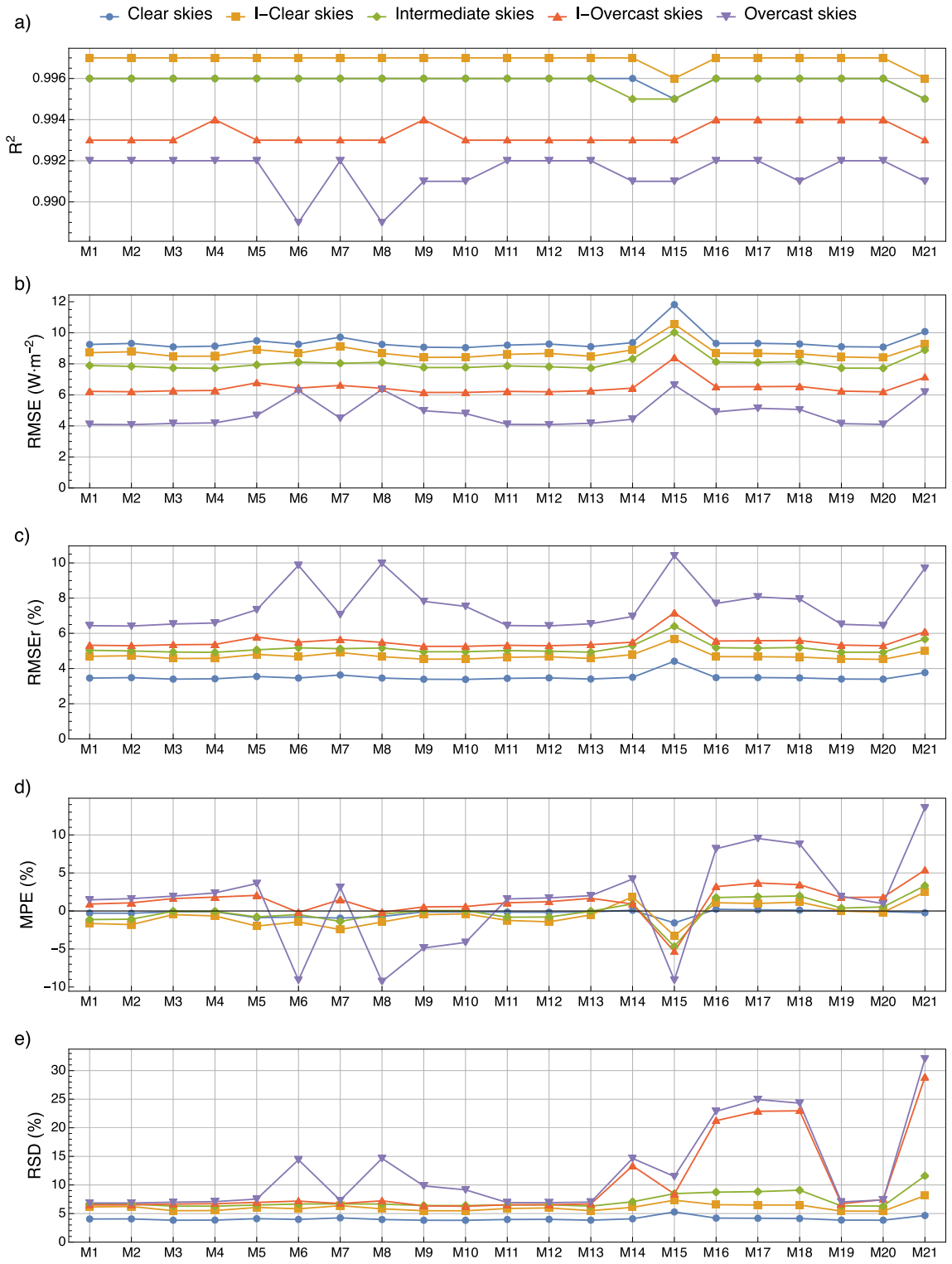

Fig. 8. Statistical errors for the five sky types and 1-min input data.

worse values up to 0.59%. For daily data the low values of *RMSEr* were maintained or slightly improved for local calibration, although the behavior of *RMSEr* was more anomalous and, in some stations like SFU, it even worsened when the models were calibrated with local data.

Regarding the other statistical errors under consideration, *MPE* is the one that improved the most when the local calibration of the models was performed. Thus, when globally calibrated models were applied, *MPE* reached values from 1% to 2% in most cases and even above 4% for some models and stations. In contrast, for local calibration

MPE reached maximum values of 0.5% in most cases and it seldom exceeded 1%.

Considering the results obtained, it can be stated that, although local calibration in general improved the quality of the estimated *PAR* values, the use of globally calibrated models provided sufficiently good results at all the analyzed locations.

4.3. Globally calibrated models evaluated by sky type

Fig. 8 shows the fit results of the *PAR* models when the measured data (Table 3) are classified into the five sky types proposed by Igawa (2014). In clear skies, which account for 53.1% of categories, the fitting errors remained small, with slightly improved percentage errors compared to those obtained when analyzing all skies together. The same was observed for intermediate clear skies (15.2% of the situations), in that the M15 and M21 model results had again somewhat worse fitting values, which was also observed for intermediate skies (21.5% of the cases). Intermediate overcast skies represent 8.5% of the total and overcast skies 1.7%. In these last two types of skies, worse *RSD*(%) and *MPE*(%) values can be seen, as well as a wider range of dispersion in the errors obtained for the different models. In clear to intermediate skies, most models tended to underestimate *PAR* values whereas in intermediate-overcast and overcast skies, the tendency was reverted and *PAR* was overestimated by most models. All models yielded higher R^2 values than 0.99 for the five sky types.

5. Conclusions

The use of a large time series including data on *PAR*, and both global and diffuse irradiance, as well as other meteorological variables, such as temperature and relative humidity, measured in the SURFRAD network of the USA at 1-min frequency, provided high quality data covering a wide range of climatic conditions. This dataset was used to calibrate 21 models previously published in the literature, to obtain *PAR* from climatic parameters that are easily measurable at weather stations.

When the globally calibrated models were applied to 1-min data, very satisfactory fitting results were achieved in all cases, with coefficients of determination above 0.99 and *RMSEr* ranging from 3.9% to 5%. When the same models were applied to hourly data, the quality of the *PAR* results obtained was maintained and the *RMSEr* values varied between 3.6% and 4.7%. In the case of daily *PAR* values, the *RMSEr* values varied between 3.33% and 6.26%. Taking account of the statistical indices, therefore, none of the reviewed models stood out from among the others.

When the *PAR* models were locally calibrated with the measured data at each station, the fit rating statistics improved slightly for most models and stations, although it was not a significant improvement that justifies the use of locally calibrated models. The selection of the globally calibrated model for the estimation of *PAR* should then be done exclusively considering the meteorological variables available in the specific location.

Although the proposed models can potentially be applied to longer time ranges than one day, it was considered that the practical results of using *PAR* values of higher temporal resolution might worsen the quality.

Finally, *PAR* radiation is expected to behave similarly at different locations when a certain sky type is present, so the models' performance for the different sky conditions could be extrapolated to any location. When sky types are taken into account, after classifying skies into five categories ranging from clear to overcast, it was observed that in the overcast skies the error statistics giving relative values worsened in the models where global irradiance was not considered or had been integrated in the linear equation (M15 to M18 and M21). Therefore, in the case of overcast skies, the use of models other than those listed above is recommended.

Funding

The authors gratefully acknowledge the financial support provided by the Spanish Ministry of Science & Innovation under the I + D+i state program "Challenges Research Projects" (Ref. RTI2018-098900-B-I00).

Credit Author Statement

Marian de Blas: Investigation, Methodology, Formal Analysis, Original draft preparation; **Ana García-Rodríguez:** Formal Analysis, Validation; Reviewing and Editing; **Ignacio García:** Investigation, Methodology, Software, Visualization; Writing- Reviewing and Editing; **José Luis Torres:** Conceptualization, Writing- Reviewing and Editing Supervision.

Declaration of Competing Interest

The authors declare that they have no known competing financial interests or personal relationships that could have appeared to influence the work reported in this paper.

Acknowledgments

We would like to thank those responsible for the SURFRAD network for making complete and quality weather data freely available to users. Open access funding provided by Universidad Pública de Navarra.

Appendix A. Prediction errors obtained by both the globally and locally calibrated models to estimate *PAR*

The errors obtained after validation of the globally and locally calibrated models for 1-min frequency are shown in Tables A.1 and A.2, respectively.

Table A.1
Prediction errors obtained by the globally calibrated M1 to M21 models when evaluated locally (for each SURFRAD station) and globally (all stations).

Model	Station	R^2	*RMSE* (Wm^{-2})	*RMSEr* (%)	*MPE* (%)	*RSD* (%)
M1	BON	0.997	9.798	4.592	1.297	5.97
	DRA	0.999	8.404	3.394	−2.916	4.94
	FPK	0.997	8.261	4.113	−2.041	5.571
	GWN	0.997	9.34	4.213	0.741	5.357
	PSU	0.997	9.514	4.892	2.305	6.087
	SXF	0.998	7.739	3.767	−1.816	4.881
	TBL	0.998	7.038	3.338	−0.49	4.477
	All stations	0.997	8.6	3.996	−0.543	5.316
M2	BON	0.997	9.831	4.607	1.19	6.002
	DRA	0.998	8.197	3.311	−2.74	4.899
	FPK	0.997	8.284	4.124	−2.	5.578
	GWN	0.997	9.439	4.258	0.516	5.426
	PSU	0.997	9.641	4.957	2.299	6.146
	SXF	0.998	7.887	3.84	−1.856	4.912
	TBL	0.998	7.131	3.382	−0.384	4.502
	All stations	0.997	8.635	4.013	−0.543	5.34
M3	BON	0.997	9.767	4.577	1.883	5.95
	DRA	0.999	8.285	3.346	−2.435	4.362
	FPK	0.997	7.986	3.976	−1.353	4.946
	GWN	0.997	9.067	4.09	1.179	5.17
	PSU	0.997	9.462	4.865	2.88	6.307
	SXF	0.998	7.52	3.661	−1.189	4.398
	TBL	0.998	6.895	3.27	0.158	4.208
	All stations	0.997	8.446	3.925	0.03	5.049
M4	BON	0.997	9.782	4.584	1.775	5.958
	DRA	0.999	8.061	3.256	−2.263	4.318
	FPK	0.997	8.026	3.996	−1.326	4.958
	GWN	0.997	9.169	4.136	0.991	5.22
	PSU	0.997	9.555	4.913	2.873	6.355
	SXF	0.998	7.673	3.735	−1.229	4.432
	TBL	0.998	6.99	3.315	0.251	4.236
	All stations	0.997	8.474	3.938	0.031	5.068
M5	BON	0.997	10.045	4.707	1.086	5.964
	DRA	0.998	8.731	3.526	−3.08	5.01
	FPK	0.997	8.635	4.299	−2.252	5.549
	GWN	0.997	9.164	4.134	0.533	5.346
	PSU	0.997	9.563	4.917	2.323	6.17
	SXF	0.998	8.12	3.953	−2.053	4.97
	TBL	0.998	7.407	3.513	−0.598	4.503
	All stations	0.997	8.816	4.097	−0.704	5.348
M6	BON	0.997	10.024	4.697	1.101	6.165
	DRA	0.999	8.569	3.461	−3.033	4.978
	FPK	0.997	8.411	4.187	−2.237	5.672
	GWN	0.997	9.063	4.088	0.221	5.503
	PSU	0.997	9.516	4.893	1.57	6.439
	SXF	0.998	7.847	3.82	−2.228	5.373
	TBL	0.998	7.265	3.446	−0.915	4.986
	All stations	0.997	8.682	4.035	−0.903	5.566
M7	BON	0.996	10.105	4.735	0.738	5.991
	DRA	0.998	8.959	3.618	−3.266	5.293
	FPK	0.997	8.908	4.435	−2.569	5.857
	GWN	0.997	9.347	4.216	0.274	5.427
	PSU	0.997	9.619	4.945	2.009	6.063
	SXF	0.998	8.379	4.079	−2.369	5.224
	TBL	0.998	7.551	3.582	−0.869	4.634
	All stations	0.997	8.987	4.176	−0.986	5.489
M8	BON	0.997	10.009	4.69	1.084	6.185
	DRA	0.998	8.427	3.404	−2.886	4.909
	FPK	0.997	8.395	4.179	−2.165	5.646
	GWN	0.997	9.101	4.105	0.137	5.555

	PSU	0.997	9.565	4.918	1.58	6.498
	SXF	0.998	7.887	3.84	−2.205	5.379
	TBL	0.998	7.282	3.454	−0.821	4.995
	All stations	0.997	8.672	4.03	−0.863	5.573
M9	BON	0.997	9.79	4.588	1.709	6.013
	DRA	0.999	8.072	3.26	−2.324	4.37
	FPK	0.997	7.964	3.965	−1.418	5.068
	GWN	0.997	9.1	4.104	0.76	5.157
	PSU	0.997	9.512	4.891	2.376	6.258
	SXF	0.998	7.549	3.675	−1.421	4.583
	TBL	0.998	6.941	3.292	−0.025	4.425
	All stations	0.997	8.431	3.918	−0.165	5.117
M10	BON	0.997	9.778	4.582	1.8	5.989
	DRA	0.999	8.244	3.33	−2.444	4.392
	FPK	0.997	7.939	3.952	−1.425	5.038
	GWN	0.997	9.034	4.075	0.934	5.099
	PSU	0.997	9.446	4.857	2.453	6.204
	SXF	0.998	7.451	3.627	−1.363	4.513
	TBL	0.998	6.875	3.261	−0.055	4.363
	All stations	0.997	8.416	3.911	−0.137	5.079
M11	BON	0.997	9.776	4.581	1.5	5.942
	DRA	0.999	8.345	3.37	−2.725	4.723
	FPK	0.997	8.172	4.068	−1.782	5.341
	GWN	0.997	9.302	4.196	0.912	5.287
	PSU	0.997	9.505	4.887	2.511	6.155
	SXF	0.998	7.68	3.739	−1.574	4.692
	TBL	0.998	6.98	3.311	−0.24	4.353
	All stations	0.997	8.553	3.975	−0.327	5.205
M12	BON	0.997	9.806	4.595	1.372	5.97
	DRA	0.998	8.13	3.284	−2.553	4.698
	FPK	0.997	8.204	4.084	−1.769	5.372
	GWN	0.997	9.4	4.24	0.671	5.351
	PSU	0.997	9.633	4.953	2.483	6.204
	SXF	0.998	7.841	3.817	−1.64	4.741
	TBL	0.998	7.082	3.359	−0.157	4.391
	All stations	0.997	8.591	3.992	−0.346	5.237
M13	BON	0.997	9.766	4.576	1.868	5.954
	DRA	0.999	8.282	3.345	−2.401	4.365
	FPK	0.997	8.012	3.988	−1.371	4.955
	GWN	0.997	9.052	4.083	1.169	5.172
	PSU	0.997	9.481	4.875	2.878	6.318
	SXF	0.998	7.538	3.67	−1.195	4.401
	TBL	0.998	6.921	3.282	0.158	4.212
	All stations	0.997	8.454	3.929	0.029	5.055
M14	BON	0.996	10.007	4.689	2.421	8.043
	DRA	0.998	9.228	3.727	−1.88	4.734
	FPK	0.997	8.281	4.123	0.	5.599
	GWN	0.997	8.557	3.86	1.26	7.155
	PSU	0.997	9.507	4.888	3.39	8.313
	SXF	0.997	7.907	3.849	−0.337	6.454
	TBL	0.998	7.873	3.734	0.851	5.968
	All stations	0.997	8.795	4.087	0.676	6.622
M15	BON	0.996	11.742	5.502	−1.079	6.821
	DRA	0.997	11.846	4.785	−4.463	7.004
	FPK	0.996	10.842	5.397	−4.108	7.596
	GWN	0.997	10.307	4.649	−2.105	6.116
	PSU	0.997	10.577	5.438	−0.912	6.506
	SXF	0.997	10.502	5.112	−4.407	7.212
	TBL	0.997	10.357	4.912	−2.908	6.471
	All stations	0.996	10.93	5.079	−2.939	6.832
M16	BON	0.996	9.968	4.671	2.554	8.862
	DRA	0.998	8.302	3.353	−1.417	5.465
	FPK	0.997	8.358	4.161	−0.157	6.939

	GWN	0.997	9.237	4.166	1.922	10.563
	PSU	0.997	9.644	4.959	4.041	11.48
	SXF	0.998	8.065	3.926	0.033	10.631
	TBL	0.998	7.373	3.497	1.448	7.777
	All stations	0.997	8.705	4.045	1.073	8.905
M17	BON	0.996	9.957	4.666	2.579	9.189
	DRA	0.998	8.325	3.363	−1.457	5.582
	FPK	0.997	8.361	4.162	−0.153	7.128
	GWN	0.997	9.221	4.159	2.004	11.199
	PSU	0.997	9.641	4.957	4.172	12.04
	SXF	0.998	8.06	3.924	0.082	11.336
	TBL	0.998	7.358	3.49	1.466	8.12
	All stations	0.997	8.702	4.044	1.107	9.341
M18	BON	0.996	9.939	4.658	2.74	9.412
	DRA	0.998	8.474	3.423	−1.656	5.454
	FPK	0.997	8.369	4.166	−0.276	7.028
	GWN	0.997	9.115	4.112	2.364	11.772
	PSU	0.997	9.569	4.92	4.173	11.997
	SXF	0.998	7.965	3.878	0.093	11.233
	TBL	0.998	7.313	3.469	1.264	7.689
	All stations	0.997	8.683	4.035	1.1	9.369
M19	BON	0.997	9.77	4.578	2.084	6.021
	DRA	0.999	8.282	3.345	−2.177	4.244
	FPK	0.997	8.002	3.984	−1.077	4.842
	GWN	0.997	8.992	4.056	1.359	5.164
	PSU	0.997	9.467	4.868	3.089	6.495
	SXF	0.998	7.546	3.673	−0.934	4.345
	TBL	0.998	6.925	3.285	0.44	4.271
	All stations	0.997	8.444	3.924	0.269	5.06
M20	BON	0.997	9.765	4.576	1.989	6.049
	DRA	0.999	8.064	3.257	−2.122	4.221
	FPK	0.997	7.953	3.959	−1.064	4.884
	GWN	0.997	9.069	4.091	1.176	5.342
	PSU	0.997	9.5	4.885	3.011	6.61
	SXF	0.998	7.566	3.683	−0.981	4.566
	TBL	0.998	6.929	3.286	0.41	4.303
	All stations	0.997	8.419	3.912	0.22	5.142
M21	BON	0.996	10.421	4.884	3.083	11.237
	DRA	0.997	10.064	4.065	−1.454	7.1
	FPK	0.996	8.969	4.465	0.919	9.049
	GWN	0.997	9.031	4.073	2.378	13.981
	PSU	0.997	9.883	5.082	5.02	14.882
	SXF	0.997	8.768	4.268	0.809	14.541
	TBL	0.997	8.66	4.107	1.941	10.559
	All stations	0.996	9.432	4.383	1.647	11.757

Table A.2
Prediction errors obtained by the locally calibrated M1 to M21 models for each SURFRAD station

Model	Station	R^2	*RMSE* (Wm^{-2})	*RMSEr* (%)	*MPE* (%)	*RSD* (%)
M1	BON	0.997	8.422	3.947	−0.38	5.679
	DRA	0.999	5.777	2.333	−0.546	3.917
	FPK	0.997	7.93	3.948	−0.701	5.155
	GWN	0.997	8.255	3.723	−0.548	5.091
	PSU	0.998	7.712	3.966	−0.253	5.658
	SXF	0.998	7.209	3.51	−0.516	4.561
	TBL	0.998	6.954	3.298	−0.501	4.473
M2	BON	0.997	8.798	4.123	−0.44	5.825
	DRA	0.999	6.408	2.588	−0.58	4.138
	FPK	0.997	7.991	3.978	−0.698	5.186
	GWN	0.997	8.907	4.017	−0.67	5.428
	PSU	0.997	8.15	4.191	−0.31	5.775
	SXF	0.998	7.346	3.576	−0.516	4.604
	TBL	0.998	7.095	3.365	−0.539	4.519
M3	BON	0.997	8.347	3.912	0.13	5.49
	DRA	0.999	5.573	2.251	0.122	3.57
	FPK	0.997	7.674	3.82	0.076	4.767
	GWN	0.997	8.063	3.636	−0.015	4.797
	PSU	0.998	7.603	3.91	0.192	5.576
	SXF	0.998	7.008	3.412	0.11	4.302
	TBL	0.998	6.823	3.236	0.101	4.207
M4	BON	0.997	8.748	4.099	0.054	5.603
	DRA	0.999	6.205	2.506	0.151	3.738
	FPK	0.997	7.745	3.855	0.058	4.789
	GWN	0.997	8.797	3.968	−0.167	5.206
	PSU	0.997	8.064	4.147	0.123	5.676
	SXF	0.998	7.155	3.483	0.084	4.325
	TBL	0.998	6.965	3.303	0.049	4.224
M5	BON	0.996	8.991	4.213	−0.6	5.8
	DRA	0.998	6.849	2.766	−0.504	4.026
	FPK	0.997	8.323	4.143	−0.985	5.234
	GWN	0.997	8.832	3.984	−0.394	5.308
	PSU	0.997	8.1	4.165	−0.14	5.711
	SXF	0.998	7.561	3.681	−0.714	4.66
	TBL	0.998	7.398	3.509	−0.758	4.519
M6	BON	0.997	8.87	4.157	−0.731	6.004
	DRA	0.999	6.4	2.585	−0.543	4.483
	FPK	0.997	8.131	4.048	−1.111	5.47
	GWN	0.997	8.666	3.908	−0.659	5.42
	PSU	0.997	8.018	4.123	−0.43	5.784
	SXF	0.998	7.36	3.583	−1.018	5.244
	TBL	0.998	7.263	3.445	−0.923	4.863
M7	BON	0.996	9.095	4.262	−0.88	5.922
	DRA	0.998	7.259	2.932	−0.958	4.268
	FPK	0.997	8.594	4.278	−1.402	5.513
	GWN	0.997	8.929	4.027	−0.713	5.371
	PSU	0.997	8.185	4.209	−0.397	5.738
	SXF	0.998	7.78	3.788	−1.059	4.819
	TBL	0.998	7.534	3.573	−0.998	4.658
M8	BON	0.997	8.766	4.108	−0.877	5.983
	DRA	0.999	6.187	2.499	−0.656	4.363
	FPK	0.997	8.13	4.047	−1.099	5.467
	GWN	0.997	8.243	3.718	−0.906	5.304
	PSU	0.998	7.741	3.981	−0.65	5.734
	SXF	0.998	7.36	3.583	−1.026	5.244
	TBL	0.998	7.261	3.444	−0.942	4.868
M9	BON	0.997	8.696	4.075	−0.116	5.685
	DRA	0.999	6.084	2.457	−0.018	3.864
	FPK	0.997	7.698	3.832	−0.104	4.874
	GWN	0.997	8.659	3.906	−0.543	5.331

	PSU	0.997	8.001	4.114	−0.216	5.721
	SXF	0.998	7.062	3.438	−0.223	4.595
	TBL	0.998	6.928	3.286	−0.108	4.328
M10	BON	0.997	8.336	3.907	0.05	5.495
	DRA	0.999	5.547	2.24	0.046	3.56
	FPK	0.997	7.64	3.803	−0.064	4.826
	GWN	0.997	8.012	3.614	−0.243	4.775
	PSU	0.998	7.58	3.898	−0.015	5.554
	SXF	0.998	6.951	3.384	−0.136	4.448
	TBL	0.998	6.805	3.227	−0.014	4.255
M11	BON	0.997	8.388	3.931	−0.159	5.588
	DRA	0.999	5.712	2.307	−0.318	3.778
	FPK	0.997	7.849	3.907	−0.378	4.984
	GWN	0.997	8.219	3.707	−0.355	4.958
	PSU	0.998	7.7	3.96	−0.102	5.623
	SXF	0.998	7.149	3.48	−0.262	4.437
	TBL	0.998	6.891	3.268	−0.256	4.353
M12	BON	0.997	8.775	4.112	−0.289	5.752
	DRA	0.999	6.349	2.564	−0.389	4.005
	FPK	0.997	7.916	3.941	−0.401	5.027
	GWN	0.997	8.888	4.009	−0.57	5.351
	PSU	0.997	8.142	4.187	−0.234	5.752
	SXF	0.998	7.299	3.553	−0.31	4.495
	TBL	0.998	7.044	3.341	−0.335	4.407
M13	BON	0.997	8.38	3.927	0.115	5.503
	DRA	0.999	5.592	2.258	0.107	3.575
	FPK	0.997	7.678	3.822	0.077	4.773
	GWN	0.997	8.089	3.648	−0.036	4.813
	PSU	0.998	7.611	3.914	0.17	5.584
	SXF	0.998	6.999	3.407	0.106	4.292
	TBL	0.998	6.825	3.237	0.095	4.202
M14	BON	0.996	8.912	4.176	0.625	8.221
	DRA	0.998	7.141	2.884	0.673	5.688
	FPK	0.997	8.216	4.09	0.565	6.301
	GWN	0.997	8.376	3.778	0.373	6.418
	PSU	0.997	7.969	4.098	0.523	7.267
	SXF	0.997	7.603	3.701	0.646	7.472
	TBL	0.998	7.867	3.731	0.793	5.893
M15	BON	0.996	10.961	5.137	−2.798	7.185
	DRA	0.997	11.167	4.51	−3.061	6.268
	FPK	0.996	10.749	5.351	−3.49	7.318
	GWN	0.997	10.214	4.607	−2.645	6.296
	PSU	0.997	9.582	4.927	−2.847	7.071
	SXF	0.997	10.03	4.883	−3.106	6.568
	TBL	0.997	10.344	4.906	−3.121	6.558
M16	BON	0.996	9.062	4.247	0.946	8.677
	DRA	0.998	7.015	2.833	0.987	7.033
	FPK	0.997	8.111	4.038	1.119	7.758
	GWN	0.997	9.064	4.088	0.966	9.719
	PSU	0.997	8.405	4.322	1.058	9.035
	SXF	0.998	7.48	3.642	1.162	10.326
	TBL	0.998	7.332	3.478	1.057	7.577
M17	BON	0.996	9.013	4.224	1.048	10.402
	DRA	0.998	6.996	2.826	1.069	7.828
	FPK	0.997	8.109	4.037	1.139	7.974
	GWN	0.997	8.983	4.052	1.144	12.878
	PSU	0.997	8.299	4.268	1.246	11.284
	SXF	0.998	7.474	3.639	1.228	11.275
	TBL	0.998	7.316	3.47	1.134	8.337
M18	BON	0.997	8.781	4.115	1.061	10.565
	DRA	0.998	6.511	2.63	1.	7.869
	FPK	0.997	8.08	4.022	1.146	8.2
	GWN	0.997	8.439	3.806	1.152	12.53

	PSU	0.997	7.982	4.104	1.253	12.001
	SXF	0.998	7.405	3.605	1.226	11.36
	TBL	0.998	7.261	3.444	1.136	8.322
M19	BON	0.997	8.405	3.939	0.343	5.538
	DRA	0.999	5.655	2.284	0.356	3.702
	FPK	0.997	7.676	3.821	0.408	4.852
	GWN	0.997	8.06	3.635	0.211	4.758
	PSU	0.998	7.617	3.917	0.327	5.622
	SXF	0.998	7.006	3.411	0.366	4.349
	TBL	0.998	6.839	3.244	0.351	4.27
M20	BON	0.997	8.69	4.072	0.148	5.586
	DRA	0.999	6.1	2.464	0.015	3.688
	FPK	0.997	7.688	3.827	0.166	4.799
	GWN	0.997	8.652	3.903	0.33	5.834
	PSU	0.997	7.981	4.104	0.2	5.724
	SXF	0.998	7.066	3.44	0.095	4.275
	TBL	0.998	6.912	3.278	0.105	4.217
M21	BON	0.996	9.491	4.448	1.435	11.097
	DRA	0.997	8.564	3.459	1.593	9.784
	FPK	0.996	8.932	4.446	1.571	9.782
	GWN	0.997	8.945	4.034	1.538	12.704
	PSU	0.997	8.468	4.354	1.579	11.47
	SXF	0.997	8.383	4.081	1.824	14.474
	TBL	0.997	8.642	4.099	1.731	10.556

Appendix B. Calibration coefficients of the models fitted from 1-min input data from each SURFRAD station

Tables B.1 to B.7 show the calibration coefficients for models M1 to M21, fitted for each station and all sky types together.

Table B.1
Calibrated models for *PAR* using 1-min input data from Bondville station (BON) and obtained determination coefficients (R^2).

Model	Calibrated expression	R^2
M1	$PAR = G\left(-0.0259244\cos^2\theta_z - 0.0260871\ln\Delta - 0.0273576\ln\varepsilon + 0.000523075T_d + 0.421399\right)$	0.9988
M2	$PAR = G\left(-0.016265\cos^2\theta_z - 0.0270273\ln\Delta - 0.0302163\ln\varepsilon + 0.423116\right)$	0.9986
M3	$PAR = G(-0.0359644\cos\theta_z - 0.0290155\ln k_T + 0.000527191T_d + 0.43095)$	0.9988
M4	$PAR = G(-0.0222549\cos\theta_z - 0.034567\ln k_T + 0.423968)$	0.9987
M5	$PAR = G(0.406094 - 0.0388095\ln k_T)$	0.9986
M6	$PAR = G\left(-0.0357595(\ln k_T)^2 - 0.0799766\ln k_T + 0.397569\right)$	0.9986
M7	$PAR = G(0.0344183\ln k_d - 0.0322647\ln\Delta + 0.411185)$	0.9985
M8	$PAR = G\left(-0.0339204(\ln k_T)^2 - 0.0764894\ln k_T + 0.000245817T_d + 0.396128\right)$	0.9986
M9	$PAR = G\left(-0.0194519\cos\theta_z - 0.0237968(\ln k_T)^2 - 0.0624967\ln k_T + 0.416044\right)$	0.9987
M10	$PAR = G\left(-0.0342295\cos\theta_z - 0.0108944(\ln k_T)^2 - 0.0419848\ln k_T + 0.000509824T_d + 0.427092\right)$	0.9988
M11	$PAR = G(-0.0361981\cos\theta_z - 0.0262882\ln\Delta - 0.0274304\ln\varepsilon + 0.00788274\ln w + 0.432731)$	0.9988
M12	$PAR = G(-0.0231224\cos\theta_z - 0.0271304\ln\Delta - 0.0302421\ln\varepsilon + 0.430717)$	0.9986
M13	$PAR = G(-0.0337806\cos\theta_z - 0.0293596\ln k_T + 0.00395218w + 0.425031)$	0.9988
M14	$PAR = (\cos\theta_z)^{0.932509}\left(-180.122k_T^3 + 216.937k_T^2 + 462.983k_T + 19.9528\right)$	0.9986
M15	$PAR = 564.298k_T\cos\theta_z$	0.9979
M16	$PAR = 0.405545G + 8.66282$	0.9927
M17	$PAR = 0.409719G - 8.91491k_T + 12.1406$	0.9928
M18	$PAR = 0.284018e + 0.40531G - 1.99409k_T + 6.35328$	0.9931
M19	$PAR = G(0.000622256e - 0.0292528\ln k_T + 0.0205566\ln m + 0.393739)$	0.9988
M20	$PAR = 0.472062G - 0.0171748G\cos\theta_z - 0.0576354Gk_T + 1.01416$	0.9933
M21	$PAR = 539.478k_T\cos\theta_z + 11.8191$	0.992

Table B.2
Calibrated models for *PAR* using 1-min input data from Desert Rock station (DRA) and obtained determination coefficients (R^2).

Model	Calibrated expression	R^2
M1	$PAR = G\left(-0.0261923\cos^2\theta_z - 0.0288812\ln\Delta - 0.0315234\ln\varepsilon + 0.000726564T_d + 0.446473\right)$	0.9996
M2	$PAR = G\left(-0.020241\cos^2\theta_z - 0.0386956\ln\Delta - 0.0416245\ln\varepsilon + 0.438563\right)$	0.9995
M3	$PAR = G(-0.036648\cos\theta_z - 0.0412194\ln k_T + 0.000712762T_d + 0.450721)$	0.9996
M4	$PAR = G(-0.0290814\cos\theta_z - 0.05102\ln k_T + 0.440383)$	0.9995
M5	$PAR = G(0.414445 - 0.0671817\ln k_T)$	0.9994
M6	$PAR = G\left(-0.0873278(\ln k_T)^2 - 0.154097\ln k_T + 0.399142\right)$	0.9995
M7	$PAR = G(0.0557939\ln k_d - 0.0528724\ln\Delta + 0.423928)$	0.9993
M8	$PAR = G\left(-0.0819571(\ln k_T)^2 - 0.145498\ln k_T + 0.000414549T_d + 0.402171\right)$	0.9995
M9	$PAR = G\left(-0.0225632\cos\theta_z - 0.0494384(\ln k_T)^2 - 0.103847\ln k_T + 0.425906\right)$	0.9995
M10	$PAR = G\left(-0.0332541\cos\theta_z - 0.0227353(\ln k_T)^2 - 0.0660267\ln k_T + 0.00067542T_d + 0.443522\right)$	0.9996
M11	$PAR = G(-0.036849\cos\theta_z - 0.0301012\ln\Delta - 0.0324425\ln\varepsilon + 0.00992457\ln w + 0.457635)$	0.9996
M12	$PAR = G(-0.0292137\cos\theta_z - 0.0393187\ln\Delta - 0.0420293\ln\varepsilon + 0.447881)$	0.9995
M13	$PAR = G(-0.0353215\cos\theta_z - 0.0411073\ln k_T + 0.00995549w + 0.438687)$	0.9996
M14	$PAR = (\cos\theta_z)^{0.933089}\left(-478.987k_T^3 + 669.882k_T^2 + 270.083k_T + 55.0193\right)$	0.9993
M15	$PAR = 582.699k_T\cos\theta_z$	0.9983
M16	$PAR = 0.415534G + 11.5006$	0.9963
M17	$PAR = 0.41783G - 6.02535k_T + 14.4017$	0.9964
M18	$PAR = 0.922787e + 0.414496G + 2.68309k_T + 5.24025$	0.9969
M19	$PAR = G(0.00161196e - 0.0408081\ln k_T + 0.0221729\ln m + 0.405402)$	0.9996
M20	$PAR = 0.522273G - 0.0265693G\cos\theta_z - 0.0896594Gk_T - 0.627671$	0.9972
M21	$PAR = 552.111k_T\cos\theta_z + 16.0335$	0.9946

Table B.3
Calibrated models for *PAR* using 1-min input data from Fort Peck station (FPK) and obtained determination coefficients (R^2).

Model	Calibrated expression	R^2
M1	$PAR = G\left(-0.0336945\cos^2\theta_z - 0.02636\ln\Delta - 0.0274589\ln\varepsilon + 0.000257494T_d + 0.439355\right)$	0.9988
M2	$PAR = G\left(-0.0300909\cos^2\theta_z - 0.0290494\ln\Delta - 0.0297221\ln\varepsilon + 0.436958\right)$	0.9988
M3	$PAR = G(-0.0425077\cos\theta_z - 0.0330176\ln k_T + 0.00027324T_d + 0.448656)$	0.9989
M4	$PAR = G(-0.0375712\cos\theta_z - 0.034241\ln k_T + 0.445954)$	0.9988
M5	$PAR = G(0.416632 - 0.0432368\ln k_T)$	0.9987
M6	$PAR = G\left(-0.0470733(\ln k_T)^2 - 0.0987647\ln k_T + 0.404925\right)$	0.9987
M7	$PAR = G(0.0368049\ln k_d - 0.0356874\ln\Delta + 0.420645)$	0.9986
M8	$PAR = G\left(-0.0470845(\ln k_T)^2 - 0.0987823\ln k_T - 0.00002874847T_d + 0.405043\right)$	0.9987
M9	$PAR = G\left(-0.0340508\cos\theta_z - 0.0237318(\ln k_T)^2 - 0.063078\ln k_T + 0.437304\right)$	0.9989
M10	$PAR = G\left(-0.0390583\cos\theta_z - 0.0202025(\ln k_T)^2 - 0.0576783\ln k_T + 0.000248194T_d + 0.441045\right)$	0.9989
M11	$PAR = G(-0.0453089\cos\theta_z - 0.0269816\ln\Delta - 0.0278478\ln\varepsilon + 0.00387382\ln w + 0.452978)$	0.9988
M12	$PAR = G(-0.0406329\cos\theta_z - 0.0296938\ln\Delta - 0.0301463\ln\varepsilon + 0.449311)$	0.9988
M13	$PAR = G(-0.041594\cos\theta_z - 0.0331143\ln k_T + 0.00279824w + 0.444784)$	0.9989
M14	$PAR = (\cos\theta_z)^{0.926626}\left(-293.565k_T^3 + 373.445k_T^2 + 409.399k_T + 27.6677\right)$	0.9987
M15	$PAR = 577.976k_T\cos\theta_z$	0.9978
M16	$PAR = 0.415314G + 9.42583$	0.9941
M17	$PAR = 0.416205G - 1.84007k_T + 10.1584$	0.9941
M18	$PAR = 0.158742e + 0.414881G - 0.340784k_T + 8.49953$	0.9941
M19	$PAR = G(0.000448402e - 0.0326234\ln k_T + 0.0242581\ln m + 0.406583)$	0.9989
M20	$PAR = 0.493898G - 0.0315763G\cos\theta_z - 0.0582316Gk_T + 0.955542$	0.9947
M21	$PAR = 550.626k_T\cos\theta_z + 12.2792$	0.9928

Table B.4
Calibrated models for *PAR* using 1-min input data from Goodwin Creek station (GWN) and obtained determination coefficients (R^2).

Model	Calibrated expression	R^2
M1	$PAR = G\left(-0.0187438\cos^2\theta_z - 0.0253306\ln\Delta - 0.0250879\ln\varepsilon + 0.000758056T_d + 0.414868\right)$	0.9989
M2	$PAR = G\left(-0.00630393\cos^2\theta_z - 0.0213583\ln\Delta - 0.0262149\ln\varepsilon + 0.425841\right)$	0.9987
M3	$PAR = G(-0.0281131\cos\theta_z - 0.0272605\ln k_T + 0.000733611T_d + 0.425694)$	0.9989
M4	$PAR = G(-0.00832906\cos\theta_z - 0.0342831\ln k_T + 0.417691)$	0.9987
M5	$PAR = G(0.410867 - 0.0356833\ln k_T)$	0.9987
M6	$PAR = G\left(-0.033815(\ln k_T)^2 - 0.0785134\ln k_T + 0.401537\right)$	0.9988
M7	$PAR = G(0.0298569\ln k_d - 0.0264207\ln\Delta + 0.41872)$	0.9987
M8	$PAR = G\left(-0.0323216(\ln k_T)^2 - 0.0741496\ln k_T + 0.000490602T_d + 0.396461\right)$	0.9989
M9	$PAR = G\left(-0.00371422\cos\theta_z - 0.0318378(\ln k_T)^2 - 0.0753847\ln k_T + 0.405126\right)$	0.9988
M10	$PAR = G\left(-0.0244533\cos\theta_z - 0.0186725(\ln k_T)^2 - 0.0517045\ln k_T + 0.000698264T_d + 0.417939\right)$	0.999
M11	$PAR = G(-0.0282613\cos\theta_z - 0.0249653\ln\Delta - 0.0247003\ln\varepsilon + 0.0115315\ln w + 0.42468)$	0.9989
M12	$PAR = G(-0.0108586\cos\theta_z - 0.0208078\ln\Delta - 0.025743\ln\varepsilon + 0.430597)$	0.9987
M13	$PAR = G(-0.0265596\cos\theta_z - 0.0271722\ln k_T + 0.00506549w + 0.419701)$	0.9989
M14	$PAR = (\cos\theta_z)^{0.947929}\left(-210.208k_T^3 + 232.516k_T^2 + 485.752k_T + 14.6498\right)$	0.9989
M15	$PAR = 571.122k_T\cos\theta_z$	0.9983
M16	$PAR = 0.411303G + 7.71913$	0.9935
M17	$PAR = 0.416971G - 10.9468k_T + 11.4661$	0.9936
M18	$PAR = 0.398187e + 0.410254G + 0.14252k_T + 1.71339$	0.9943
M19	$PAR = G(0.000818772e - 0.0267586\ln k_T + 0.018002\ln m + 0.394531)$	0.9989
M20	$PAR = 0.456942G + 0.00166113G\cos\theta_z - 0.0545554Gk_T + 2.81898$	0.9941
M21	$PAR = 549.744k_T\cos\theta_z + 10.5202$	0.9937

Table B.5
Calibrated models for *PAR* using 1-min input data from Penn. State University station (PSU) and obtained determination coefficients (R^2).

Model	Calibrated expression	R^2
M1	$PAR = G\left(-0.0166701\cos^2\theta_z - 0.0250514\ln\Delta - 0.0252981\ln\varepsilon + 0.000556096T_d + 0.414047\right)$	0.9988
M2	$PAR = G\left(-0.00673068\cos^2\theta_z - 0.0238131\ln\Delta - 0.0264715\ln\varepsilon + 0.416307\right)$	0.9987
M3	$PAR = G(-0.0229097\cos\theta_z - 0.0264228\ln k_T + 0.000550073T_d + 0.421451)$	0.9988
M4	$PAR = G(-0.00890567\cos\theta_z - 0.0299549\ln k_T + 0.414148)$	0.9987
M5	$PAR = G(0.407185 - 0.0310584\ln k_T)$	0.9987
M6	$PAR = G\left(-0.0201476(\ln k_T)^2 - 0.0575878\ln k_T + 0.401414\right)$	0.9987
M7	$PAR = G(0.027987\ln k_d - 0.0260995\ln\Delta + 0.411151)$	0.9986
M8	$PAR = G\left(-0.0185985(\ln k_T)^2 - 0.0542781\ln k_T + 0.000388764T_d + 0.39928\right)$	0.9988
M9	$PAR = G\left(-0.00621358\cos\theta_z - 0.0180068(\ln k_T)^2 - 0.0539991\ln k_T + 0.406885\right)$	0.9987
M10	$PAR = G\left(-0.0208019\cos\theta_z - 0.0108647(\ln k_T)^2 - 0.0410521\ln k_T + 0.000531084T_d + 0.416817\right)$	0.9988
M11	$PAR = G(-0.0232898\cos\theta_z - 0.0249902\ln\Delta - 0.0251929\ln\varepsilon + 0.00811827\ln w + 0.42153)$	0.9988
M12	$PAR = G(-0.00996949\cos\theta_z - 0.02376\ln\Delta - 0.0263967\ln\varepsilon + 0.419806)$	0.9987
M13	$PAR = G(-0.0214083\cos\theta_z - 0.0264027\ln k_T + 0.0049105w + 0.414311)$	0.9988
M14	$PAR = (\cos\theta_z)^{0.954153}\left(-194.753k_T^3 + 222.936k_T^2 + 474.176k_T + 16.2113\right)$	0.9987
M15	$PAR = 563.059k_T\cos\theta_z$	0.9981
M16	$PAR = 0.407821G + 6.43092$	0.9941
M17	$PAR = 0.414188G - 10.7777k_T + 9.67382$	0.9942
M18	$PAR = 0.34763e + 0.409569G - 5.06873k_T + 4.50106$	0.9946
M19	$PAR = G(0.000792017e - 0.0263632\ln k_T + 0.0131349\ln m + 0.394484)$	0.9988
M20	$PAR = 0.457128G - 0.00352162G\cos\theta_z - 0.052867Gk_T + 0.992148$	0.9946
M21	$PAR = 543.701k_T\cos\theta_z + 8.87978$	0.994

Table B.6
Calibrated models for *PAR* using 1-min input data from Sioux Falls station (SXF) and obtained determination coefficients (R^2).

Model	Calibrated expression	R^2
M1	$PAR = G(-0.0270748\cos^2\theta_z - 0.0233918\ln\Delta - 0.0244928\ln\varepsilon + 0.000301957T_d + 0.437978)$	0.999
M2	$PAR = G(-0.0208262\cos^2\theta_z - 0.0263429\ln\Delta - 0.0274028\ln\varepsilon + 0.435804)$	0.999
M3	$PAR = G(-0.0359149\cos\theta_z - 0.0290881\ln k_T + 0.000307922T_d + 0.446052)$	0.9991
M4	$PAR = G(-0.0274843\cos\theta_z - 0.031694\ln k_T + 0.441531)$	0.999
M5	$PAR = G(0.419954 - 0.0372785\ln k_T)$	0.9989
M6	$PAR = G\left(-0.0408875(\ln k_T)^2 - 0.0870585\ln k_T + 0.409132\right)$	0.999
M7	$PAR = G(0.0319198\ln k_d - 0.0311002\ln\Delta + 0.423177)$	0.9989
M8	$PAR = G\left(-0.0408183(\ln k_T)^2 - 0.0869378\ln k_T + 0.0000125502T_d + 0.409064\right)$	0.999
M9	$PAR = G\left(-0.0240868\cos\theta_z - 0.0280449(\ln k_T)^2 - 0.0665285\ln k_T + 0.431441\right)$	0.9991
M10	$PAR = G\left(-0.0322136\cos\theta_z - 0.0222174(\ln k_T)^2 - 0.0569965\ln k_T + 0.000271039T_d + 0.437517\right)$	0.9991
M11	$PAR = G(-0.0374632\cos\theta_z - 0.0237178\ln\Delta - 0.0246503\ln\varepsilon + 0.00465075\ln w + 0.449544)$	0.9991
M12	$PAR = G(-0.0289148\cos\theta_z - 0.0267004\ln\Delta - 0.0276172\ln\varepsilon + 0.444885)$	0.999
M13	$PAR = G(-0.0348077\cos\theta_z - 0.0291257\ln k_T + 0.0026568w + 0.442077)$	0.9991
M14	$PAR = (\cos\theta_z)^{0.929967}(-291.019k_T^3 + 364.55k_T^2 + 426.772k_T + 22.5131)$	0.9989
M15	$PAR = 582.089k_T\cos\theta_z$	0.9981
M16	$PAR = 0.419434G + 8.05983$	0.9952
M17	$PAR = 0.420718G - 2.61838k_T + 9.06978$	0.9952
M18	$PAR = 0.154547e + 0.418294G + 0.383924k_T + 6.65462$	0.9953
M19	$PAR = G(0.000421147e - 0.0287839\ln k_T + 0.0207711\ln m + 0.409903)$	0.9991
M20	$PAR = 0.490487G - 0.0238271G\cos\theta_z - 0.0574915Gk_T + 0.434208$	0.9957
M21	$PAR = 557.054k_T\cos\theta_z + 11.3821$	0.9939

Table B.7
Calibrated models for *PAR* using 1-min input data from Table Mountain station (TBL) and obtained determination coefficients (R^2).

Model	Calibrated expression	R^2
M1	$PAR = G(-0.023619\cos^2\theta_z - 0.0276188\ln\Delta - 0.0277975\ln\varepsilon + 0.00035631T_d + 0.428664)$	0.9992
M2	$PAR = G(-0.0183781\cos^2\theta_z - 0.0287877\ln\Delta - 0.0292228\ln\varepsilon + 0.426524)$	0.9991
M3	$PAR = G(-0.0325096\cos\theta_z - 0.0287528\ln k_T + 0.000351184T_d + 0.439248)$	0.9992
M4	$PAR = G(-0.0256534\cos\theta_z - 0.030557\ln k_T + 0.434464)$	0.9991
M5	$PAR = G(0.414619 - 0.0348299\ln k_T)$	0.999
M6	$PAR = G\left(-0.0303389(\ln k_T)^2 - 0.0713085\ln k_T + 0.407652\right)$	0.9991
M7	$PAR = G(0.0334245\ln k_d - 0.0336848\ln\Delta + 0.414363)$	0.999
M8	$PAR = G\left(-0.0303117(\ln k_T)^2 - 0.0712003\ln k_T + 0.0000400073T_d + 0.407599\right)$	0.9991
M9	$PAR = G\left(-0.0234503\cos\theta_z - 0.0159809(\ln k_T)^2 - 0.0501389\ln k_T + 0.42909\right)$	0.9992
M10	$PAR = G\left(-0.0305593\cos\theta_z - 0.0114026(\ln k_T)^2 - 0.0428243\ln k_T + 0.000331802T_d + 0.43515\right)$	0.9992
M11	$PAR = G(-0.0330803\cos\theta_z - 0.0281437\ln\Delta - 0.028116\ln\varepsilon + 0.00517464\ln w + 0.438895)$	0.9992
M12	$PAR = G(-0.0261265\cos\theta_z - 0.029134\ln\Delta - 0.0294361\ln\varepsilon + 0.434904)$	0.9991
M13	$PAR = G(-0.0317435\cos\theta_z - 0.0288389\ln k_T + 0.00401612w + 0.433972)$	0.9992
M14	$PAR = (\cos\theta_z)^{0.929085}(-142.691k_T^3 + 166.044k_T^2 + 494.632k_T + 15.9574)$	0.9989
M15	$PAR = 573.024k_T\cos\theta_z$	0.9981
M16	$PAR = 0.412172G + 8.21022$	0.9958
M17	$PAR = 0.414113G - 3.93812k_T + 9.77532$	0.9958
M18	$PAR = 0.236214e + 0.412381G - 1.72243k_T + 7.49131$	0.9958
M19	$PAR = G(0.000623222e - 0.0285695\ln k_T + 0.0191117\ln m + 0.404614)$	0.9992
M20	$PAR = 0.478529G - 0.0213716G\cos\theta_z - 0.0519381Gk_T + 0.729894$	0.9962
M21	$PAR = 548.87k_T\cos\theta_z + 11.5596$	0.9941

References

Aguiar, L.J.G., Fischer, G.R., Ladle, R.J., Malhado, A.C.M., Justino, F. B., Aguiar, R.G., da Costa, J.M.N., 2012. Modeling the photosynthetically active radiation in South West Amazonia under all sky conditions. Theoret. Appl. Climatol. 108, 631–640. https://doi.org/10.1007/s00704-011-0556-z.

Akitsu, T., Kume, A., Hirose, Y., Ijima, O., Nasahara, K.N., 2015. On the stability of radiometric ratios of photosynthetically active radiation to global solar radiation in Tsukuba, Japan. Agric. For. Meteorol. 209, 59–68. https://doi.org/10.1016/j.agrformet.2015.04.026.

Alados, I., Foyo-Moreno, I., Alados-Arboledas, L., 1996. Photosynthetically active radiation: measurements and modelling. Agric. For. Meteorol. 78, 121–131. https://doi.org/10.1016/0168-1923(95)02245-7.

Awal, M., Koshi, H., Ikeda, T., 2006. Radiation interception and use by maize/peanut intercrop canopy. Agric. For. Meteorol. 139, 74–83. https://doi.org/10.1016/j.agrformet.2006.06.001.

Beck, H.E., Zimmermann, N.E., McVicar, T.R., Vergopolan, N., Berg, A., Wood, E.F., 2018. Present and future Köppen-Geiger climate classification maps at 1-km resolution. Scientific Data 5, 180214. https://doi.org/10.1038/sdata.2018.214.

Bhattacharya, A., 2019. Radiation-Use Efficiency Under Different Climatic Conditions. In: Changing Climate and Resource Use Efficiency in Plants, Elsevier, 2019, pp. 51–109. https://doi.org/10.1016/B978-0-12-816209-5.00002-7. URL: https://linkinghub.elsevier.com/retrieve/pii/B9780128162095000027.

Bredmose, N., Costes, E., 2017. Axillary Bud Growth. In: Reference Module in Life Sciences, Elsevier, 2017. https://doi.org/10.1016/B978-0-12-809633-8.05056-1. URL: https://www.sciencedirect.com/science/article/pii/B9780128096338050561, https://linkinghub.elsevier.com/retrieve/pii/B9780128096338050561.

Campillo, C., Fortes, R., del Henar Prieto, M., 2012. Solar Radiation Effect on Crop Production. In: Solar Radiation, figure 1, InTech, https://doi.org/10.5772/34796. URL: http://www.intechopen.com/books/solar-radiation/solar-radiation-effect-on-crop-production.

Dauzat, J., Eroy, M., 1997. Simulating light regime and intercrop yields in coconut based farming systems. In: Developments in Crop Science, vol. 25, Elsevier, 1997, pp. 87–98. https://doi.org/10.1016/S0378-519X(97)80011-6. URL: https://www.sciencedirect.com/science/article/pii/S0378519X97800116, https://linkinghub.elsevier.com/retrieve/pii/S0378519X97800116.

Ferrera-Cobos, F., Vindel, J., Valenzuela, R., González, J., 2020. Models for estimating daily photosynthetically active radiation in oceanic and mediterranean climates and their improvement by site adaptation techniques. Adv. Space Res. 65, 1894–1909. https://doi.org/10.1016/j.asr.2020.01.018.

Foyo-Moreno, I., Alados, I., Alados-Arboledas, L., 2017. A new conventional regression model to estimate hourly photosynthetic photon flux density under all sky conditions. Int. J. Climatol. 37, 1067–1075. https://doi.org/10.1002/joc.5063.

García-Rodríguez, A., García-Rodríguez, S., Díez-Mediavilla, M., Alonso-Tristán, C., 2020. Photosynthetic active radiation, solar irradiance and the cie standard sky classification. Appl. Sci. (Switzerland) 10, 1–14. https://doi.org/10.3390/app10228007.

García-Rodríguez, A., Granados-López, D., García-Rodríguez, S., Díez-Mediavilla, M., Alonso-Tristán, C., 2021. Agricultural and Forest Meteorology Modelling Photosynthetic Active Radiation (PAR) through meteorological indices under all sky conditions. Agric. For. Meteorol. 310. https://doi.org/10.1016/j.agrformet.2021.108627.

Ge, S., Smith, R.G., Jacovides, C.P., Kramer, M.G., Carruthers, R.I., 2011. Dynamics of photosynthetic photon flux density (PPFD) and estimates in coastal northern California. Theoret. Appl. Climatol. 105, 107–118. https://doi.org/10.1007/s00704-010-0368-6.

Gueymard, C.A., 2018. A reevaluation of the solar constant based on a 42-year total solar irradiance time series and a reconciliation of spaceborne observations. Sol. Energy 168, 2–9. https://doi.org/10.1016/j.solener.2018.04.001.

Gueymard, C., Myers, D., Emery, K., 2002. Proposed reference irradiance spectra for solar energy systems testing. Sol. Energy 73, 443–467. https://doi.org/10.1016/S0038-092X(03)00005-7.

Hao, D., Asrar, G.R., Zeng, Y., Zhu, Q., Wen, J., Xiao, Q., Chen, M., 2020. DSCOVR/EPIC-derived global hourly and daily downward shortwave and photosynthetically active radiation data at 0.1° x 0.1° resolution. Earth Syst. Sci. Data 12, 2209–2221. https://doi.org/10.5194/essd-12-2209-2020.

Hu, B., Wang, Y., Liu, G., 2007. Measurements and estimations of photosynthetically active radiation in Beijing. Atmos. Res. 85, 361–371. https://doi.org/10.1016/j.atmosres.2007.02.005.

IEC, 2019. IEC 60904-3: 2019. Photovoltaic devices - Part 3: Measurement principles for terrestrial photovoltaic (PV) solar devices with reference spectral irradiance data, Technical Report, International Electrotechnical Commission.

Igawa, N., 2014. Improving the All Sky Model for the luminance and radiance distributions of the sky. Sol. Energy 105, 354–372. https://doi.org/10.1016/j.solener.2014.03.020.

Jacovides, C., Tymvios, F., Assimakopoulos, V., Kaltsounides, N., 2007. The dependence of global and diffuse PAR radiation components on sky conditions at Athens, Greece. Agric. For. Meteorol. 143, 277–287. https://doi.org/10.1016/j.agrformet.2007.01.004.

Jacovides, C., Tymvios, F., Boland, J., Tsitouri, M., 2015. Artificial Neural Network models for estimating daily solar global UV, PAR and broadband radiant fluxes in an eastern Mediterranean site. Atmos. Res. 152, 138–145. https://doi.org/10.1016/j.atmosres.2013.11.004.

Jajoo, A., Ladle, R.J., Zivcak, M., Łukasik, I., Goltsev, V., Brestic, M., Oukarroum, A., Dbrowski, P., Ahmad, P., Samborska, I.A., Cetner, M.D., Kalaji, H.M., 2014. The Use of Chlorophyll Fluorescence Kinetics Analysis to Study the Performance of Photosynthetic Machinery in Plants. In: Emerging Technologies and Management of Crop Stress Tolerance, Academic Press, pp. 347–384. https://doi.org/10.1016/b978-0-12-800875-1.00015-6. URL: https://www.sciencedirect.com/science/article/pii/B9780128008751000156.

Janjai, S., Wattan, R., Sripradit, A., 2015. Modeling the ratio of photosynthetically active radiation to broadband global solar radiation using ground and satellite-based data in the tropics. Adv. Space Res. 56, 2356–2364. https://doi.org/10.1016/j.asr.2015.09.020.

Kasten, F., Young, A.T., 1989. Revised optical air mass tables and approximation formula. Appl. Opt. 28, 4735. https://doi.org/10.1364/AO.28.004735.

Leckner, B., 1978. The spectral distribution of solar radiation at the earth's surface–elements of a model. Sol. Energy 20, 143–150. https://doi.org/10.1016/0038-092X(78)90187-1.

Li, R., Zhao, L., Ding, Y., Wang, S., Ji, G., Xiao, Y., Liu, G., Sun, L., 2010. Monthly ratios of PAR to global solar radiation measured at northern Tibetan Plateau, China. Sol. Energy 84, 964–973. https://doi.org/10.1016/j.solener.2010.03.005.

Li, L., Xin, X., Zhang, H., Yu, J., Liu, Q., Yu, S., Wen, J., 2015. A method for estimating hourly photosynthetically active radiation (PAR) in China by combining geostationary and polar-orbiting satellite data. Remote Sens. Environ. 165, 14–26. https://doi.org/10.1016/j.rse.2015.03.034.

Liu, X., Rahman, T., Song, C., Yang, F., Su, B., Cui, L., Bu, W., Yang, W., 2018. Relationships among light distribution, radiation use efficiency and land equivalent ratio in maize-soybean strip intercropping. Field Crops Res. 224, 91–101. https://doi.org/10.1016/J.FCR.2018.05.010.

Long, C., Dutton, E., 2002. BSRN Global Network Recommended QC Tests, v2.0. In: Report No 1–3, Baseline Surface Radiation Network.

McCree, K., 1972. Test of current definitions of photosynthetically active radiation against leaf photosynthesis data. Agric. Meteorol. 10, 443–453. https://doi.org/10.1016/0002-1571(72)90045-3.

Mizoguchi, Y., Ohtani, Y., Aoshima, T., Hirakata, A., Yuta, S., Takanashi, S., Iwata, H., Nakai, Y., 2010. Comparison of the characteristics of five quantum sensors. Bull. FFPRI 9, 113–120.

Mizoguchi, Y., Yasuda, Y., Ohtani, Y., Watanabe, T., Kominami, Y., Yamanoi, K., 2014. A practical model to estimate photosynthetically

active radiation using general meteorological elements in a temperate humid area and comparison among models. Theoret. Appl. Climatol. 115, 583–589. https://doi.org/10.1007/s00704-013-0912-2.

Mottus, M., Sulev, M., Baret, F., Lopez-Lozano, R., Reinart, A., 2012. Photosynthetically Active Radiation: Measurement photosynthesis/photosynthetic(ally) active radiation (PAR) measurement and Modeling photosynthesis/photosynthetic(ally) active radiation (PAR) modeling. In: Meyers, R.A. (Ed.), Encyclopedia of Sustainability Science and Technology, Springer, New York, New York, NY, 2012, pp. 7902–7932. https://doi.org/10.1007/978-1-4419-0851-3_451. URL. http://link.springer.com/10.1007/978-1-4419-0851-3_451.

Nwokolo, S., Amadi, S., 2018. A Global Review of Empirical Models for Estimating Photosynthetically Active Radiation. Trends Renew. Energy 4, 236–327. https://doi.org/10.17737/tre.2018.4.2.0079.

Ogburn, R.M., Edwards, E.J., 2010. The Ecological Water-Use Strategies of Succulent Plants. In: Advances in Botanical Research, vol. 55, Academic Press, pp. 179–225. https://doi.org/10.1016/B978-0-12-380868-4.00004-1. URL: https://www.sciencedirect.com/science/article/pii/B9780123808684000041, https://linkinghub.elsevier.com/retrieve/pii/B9780123808684000041.

O'Gorman, E.J., Pichler, D.E., Adams, G., Benstead, J.P., Cohen, H., Craig, N., Cross, W.F., Demars, B.O., Friberg, N., Gíslason, G.M., Gudmundsdóttir, R., Hawczak, A., Hood, J.M., Hudson, L.N., Johansson, L., Johansson, M.P., Junker, J.R., Laurila, A., Manson, J.R., Mavromati, E., Nelson, D., Ólafsson, J.S., Perkins, D.M., Petchey, O.L., Plebani, M., Reuman, D.C., Rall, B.C., Stewart, R., Thompson, M.S., Woodward, G., 2012. Impacts of Warming on the Structure and Functioning of Aquatic Communities. In: Woodward, G., Jacob, U., O'Gorman, E.J.B.T.A.I.E.R. (Eds.), Advances in Ecological Research, vol. 47. Academic Press. https://doi.org/10.1016/B978-0-12-398315-2.00002-8, URL: https://www.sciencedirect.com/science/article/pii/B9780123983152000028, https://linkinghub.elsevier.com/retrieve/pii/B9780123983152000028.

Peng, S., 2000. Single-leaf and canopy photosynthesis of rice11Citation: Sheehy JE, Mitchell PL, Hardy B, editors. 2000. Redesigning rice photosynthesis to increase yield. Proceedings of the Workshop on The Quest to Reduce Hunger: Redesigning Rice Photosynthesis, 30 Nov. In: Studies in Plant Science, vol. 7, Elsevier, 2000, pp. 213–228. URL: https://www.sciencedirect.com/science/article/pii/S0928342000800178, https://linkinghub.elsevier.com/retrieve/pii/S0928342000800178. https://doi.org/10.1016/S0928-3420(00)80017-8.

Perez, R., Ineichen, P., Seals, R., Michalsky, J.J., Stewart, R., 1990. Modeling daylight availability and irradiance components from direct and global irradiance. Sol. Energy 44, 271–289. https://doi.org/10.1016/0038-092X(90)90055-H.

Rahman, M.M., Stanley, J.N., Lamb, D.W., Trotter, M.G., 2014. Methodology for measuring fAPAR in crops using a combination of active optical and linear irradiance sensors: a case study in Triticale (X Triticosecale Wittmack). Precision Agric. 15, 532–542. https://doi.org/10.1007/s11119-014-9349-6.

Ross, J., Sulev, M., 2000. Sources of errors in measurements of PAR. Agric. For. Meteorol. 100, 103–125. https://doi.org/10.1016/S0168-1923(99)00144-6.

Sun, Z., Liang, H., Liu, J., Shi, G., 2017. Estimation of photosynthetically active radiation using solar radiation in the UV–visible spectral band. Sol. Energy 153, 611–622. https://doi.org/10.1016/j.solener.2017.06.007.

Tang, W., Qin, J., Yang, K., Niu, X., Min, M., Liang, S., 2017. An efficient algorithm for calculating photosynthetically active radiation with MODIS products. Remote Sens. Environ. 194, 146–154. https://doi.org/10.1016/j.rse.2017.03.028.

Torres, A.P., Lopez, R.G., 2012. Measuring Daily Light Integral in a Greenhouse Commercial Greenhouse Production Purdue extension HO-238-W, URL: www.hort.purdue.edu.

Vindel, J.M., Valenzuela, R.X., Navarro, A.A., Zarzalejo, L.F., Paz-Gallardo, A., Souto, J.A., Méndez-Gómez, R., Cartelle, D., Casares, J. J., 2018. Modeling photosynthetically active radiation from satellite-derived estimations over mainland spain. Remote Sens. 10, 1–13. https://doi.org/10.3390/rs10060849.

Vindel, J., Valenzuela, R., Navarro, A., Zarzalejo, L., 2018. Methodology for optimizing a photosynthetically active radiation monitoring network from satellite-derived estimations: A case study over mainland Spain. Atmos. Res. 212, 227–239. https://doi.org/10.1016/j.atmosres.2018.05.010.

Wandji Nyamsi, W., Espinar, B., Blanc, P., Wald, L., 2015. Estimating the photosynthetically active radiation under clear skies by means of a new approach. Adv. Sci. Res. 12, 5–10. https://doi.org/10.5194/asr-12-5-2015.

Wandji Nyamsi, W., Blanc, P., Augustine, J.A., Arola, A., Wald, L., 2019. A New Clear-Sky Method for Assessing Photosynthetically Active Radiation at the Surface Level. Atmosphere 10, 219. https://doi.org/10.3390/atmos10040219.

Wang, L., Gong, W., Li, C., Lin, A., Hu, B., Ma, Y., 1961. Measurement and estimation of photosynthetically active radiation from 1961 to 2011 in Central China. Appl. Energy 111 (2013), 1010–1017. https://doi.org/10.1016/j.apenergy.2013.07.001.

Wang, L., Kisi, O., Zounemat-Kermani, M., Hu, B., Gong, W., 2016. Modeling and comparison of hourly photosynthetically active radiation in different ecosystems. Renew. Sustain. Energy Rev. 56, 436–453. https://doi.org/10.1016/j.rser.2015.11.068.

Yu, X., Wu, Z., Jiang, W., Guo, X., 2015. Predicting daily photosynthetically active radiation from global solar radiation in the Contiguous United States. Energy Convers. Manage. 89, 71–82. https://doi.org/10.1016/j.enconman.2014.09.038.

Zempila, M.M., Taylor, M., Bais, A., Kazadzis, S., 2016. Modeling the relationship between photosynthetically active radiation and global horizontal irradiance using singular spectrum analysis. J. Quant. Spectrosc. Radiat. Transfer 182, 240–263. https://doi.org/10.1016/j.jqsrt.2016.06.003.

Zhang, L., van der Werf, W., Bastiaans, L., Zhang, S., Li, B., Spiertz, J., 2008. Light interception and utilization in relay intercrops of wheat and cotton. Field Crops Res. 107, 29–42. https://doi.org/10.1016/j.fcr.2007.12.014.